FINITE ELEMENT STUDIES OF ORTHOGONAL MACHINING OF AISI 1045 STEEL

by

Parth N. Thekdi

A thesis submitted to the faculty of
The University of North Carolina at Charlotte
in partial fulfillment of the requirements
for the degree of Master of Science in
Mechanical Engineering

Charlotte

2019

Approved by:

_____
Dr. Harish P. Cherukuri

_____
Dr. Ronald E. Smelser

_____
Dr. Praveen Ramaprabhu

ABSTRACT

PARTH N. THEKDI. Finite Element Studies of Orthogonal Machining of AISI 1045 Steel. (Under the direction of DR. HARISH P. CHERUKURI)

In this work, a two-dimensional finite element model of orthogonal machining of AISI 1045 steel is developed using the commercial non-linear finite element package ABAQUS. The material behavior is described using the Johnson-Cook constitutive law. Furthermore, the Johnson-Cook damage model for damage initiation and Hillerborg's model with fracture toughness values are used for damage evolution. The fracture-based approach outlined by Patel and Cherukuri in a previous work is used for chip separation and serration. The friction conditions between the cutting tool and chip are captured using a stress-based criterion.

The predictions from the model are validated by comparing with the experimental results available in the literature for 1045 steel. Once validated, various parametric studies are conducted to study the process parameter effect on cutting forces and tool-chip interfaces. The results from the parametric studies are compared with experimental results to further validate the fracture-based approach for cutting simulations. In addition, since multiple sets of values for the Johnson-Cook parameters are quoted in the literature for 1045 steel, the effect of these different sets on cutting forces is also studied.

It is found that the model is capable of predicting accurate cutting forces and tool-chip interface temperatures. However, it does not predict the chip shapes accurately. Further refinement of the fracture models using a combined experimental and theoretical work is needed to improve on the chip shape predictions.

DEDICATION

I would like to dedicate my master's thesis to my family NitinKumar Thekdi, Hetalben Thekdi, Gunjan Thekdi, Suryaben Thekdi, Hasmukh Thekdi, Devila Thekdi and Mugdha Shah.

ACKNOWLEDGEMENTS

I would like to express my gratitude to my advisor Dr. Harish Cherukuri, for his continuous support, motivation, and guidance in helping me throughout my research and writing of this thesis. His guidance always inspired me and brought me to a higher level of thinking.

I would also like to thank Dr. Ronald Smelser and Dr. Praveen Ramaprabhu for serving on my thesis committee.

I would like to give special thanks to Jaimeen Patel for guiding me throughout my thesis and for providing valuable insight and knowledge. I would also like to thank Manish Mekarthy, Nishant Ojal, Vrushank Balutkar and other fellow lab-members for their valuable guidance and help during this thesis work.

Last but not least, I would like to give a big thank you to my family for their continuous support, love, and encouragement.

TABLE OF CONTENTS

LIST OF TABLES

LIST OF FIGURES

LIST OF ABBREVIATIONS

α	Tool rake angle
α_c	Tool clearance angle
$\bar{\sigma}$	Equivalent stress
$\bar{\varepsilon}^{pl}$	Equivalent plastic strain
$\bar{\varepsilon}_f^{pl}$	Equivalent plastic strain at failure
$\dot{\bar{\varepsilon}}^{pl}$	Equivalent plastic strain rate
$\dot{\bar{\varepsilon}}_0$	Reference strain rate
μ	Friction coefficient
ϕ	Shear plane angle
τ_{p}	Limiting shear stress
a_c	Uncut chip thickness
a_{ch}	Chip thickness after cutting
d_1	Initial failure strain
d_2	Exponential factor
d_3	Triaxiality factor
d_4	Strain rate factor
d_5	Temperature factors measured at or below T_{trans}
F_c	Cutting force
F_t	Trust force
G_{f}	Fracture toughnes
$G_{\mathrm{f}}^{\mathrm{sep}}$	Fracture toughness of chip separation
$G_{\mathrm{f}}^{\mathrm{serr}}$	Fracture toughness of chip serration
T_{trans}	Transition temperature

T_{melt} Melting temperature

V_c Cutting velocity

V_f Chip sliding velocity

A Initial yield stress

ANN Artificial Neural Network

B Hardening modulus

BUE Build Up Edge

C Strain rate dependency coefficient

FE Finite Element

FEM Finite Element Method

m Thermal softening coefficient

n Work-Hardening exponent

SVM Support Vector Machine

WRM Weighted Residual Method

CHAPTER 1: INTRODUCTION

1.1 Background

In the modern age, high-speed machining is essential as an advanced manufacturing technology. Machining has developed over the past five decades and has helped to improve the efficiency of production, reduce cost, and improve the quality of a machined surface.

Machining is a widely used material removal process to remove unwanted material from the workpiece and to achieve dimensional accuracy and a desired surface finish for further assembly operations. Machining is a complex process due to its a large plastic deformation in concentrated zones, higher cutting temperatures, and friction at the tool-chip interface. Accurate prediction of displacement, stress, strain, temperature fields, and cutting force distribution in the metal cutting process are difficult to obtain due to the non-linearity and time-dependency of the process. Identifying these parameters is vital to optimize cutting conditions, tool material, tool coating, surface accuracy, and productivity.

As a result of the complexity in the machining process, the finite element (FE) approach is accepted by researchers for predicting machining results. The challenging part in FE simulation is to obtain accurate material separation criteria while cutting. Several techniques were introduced by numerous researchers and are discussed in the literature. Also, friction between the tool and workpiece at the tool-chip interface is a highly complex phenomena in metal cutting.

1.2 Objective of Study

Machining is a common phenomenon in the industry; however, it requires trial and error for process optimization. So, the finite element approach can help in the prediction of variables that minimize time-consuming and extensive experimental procedures.

The main objective of this study is to develop a two-dimensional finite element model of the orthogonal metal cutting operation and to establish a predictive theory that would enable the evaluation of various parameters without expensive cutting experiments. Parametric studies are conducted for different cutting and finite element model parameters. Cutting parameters can be varied including tool rake angle, cutting speed, and uncut chip thickness. Finite element model parameters contain different constitutive models, chip separation criteria, and other modeling related parameters. At the end of the simulations, cutting forces, tool-chip temperature at interfaces, equivalent plastic strain, and von-Mises stress are study and observed with this model. The effect of two different sets of the Johnson-Cook damage parameters are also observed in this study, and a new machining model based on fracture mechanics concepts for material separation is presented. Results of this model are verified with the experiment results from the literature.

CHAPTER 2: LITERATURE REVIEW

2.1 Basics of Orthogonal Machining

Machining is broadly classified into two different types, conventional and non-conventional, based on the machining kinematics. Conventional machining includes turning, milling, trimming, drilling, and abrasive cutting. Non-conventional machining includes abrasive water jet machining, laser machining, and others.

Conventional machining can be further divided into orthogonal and oblique cutting, based on the feed angle and cutting direction of the tool. Orthogonal machining is a metal cutting process in which the cutting edge of the cutting tool is perpendicular to the direction of the feed motion. It represents a two-dimensional mechanical problem with no side curling of the chip. A small portion of the end turning of a thin-wall tube can be considered for this type of representation. Because of its two-dimensional representation, orthogonal machining eliminates many independent variables; for example, cutting force in the third direction is ignored. On the other side, oblique cutting is a type of cutting when the cutting tool is inclined to the direction of the feed motion, and it corresponds to the three-dimensional problems with more practical chip flow representation. This representation is more complex and needs to consider all three force components in the cutting analysis.

In this study, we will consider orthogonal machining as shown in Fig. 2.1 which illustrates the orthogonal cutting process [1]. In this figure, a_{c} is uncut chip thickness, a_{ch} is chip thickness after material separation, α is a rake angle, ϕ is a shear plane angle, V_{c} is a cutting velocity, V_{f} is a chip sliding velocity, F_{c} is a cutting force, and F_{t} is represented as a thrust force.

During machining, the workpiece material plastically deforms and creates shear

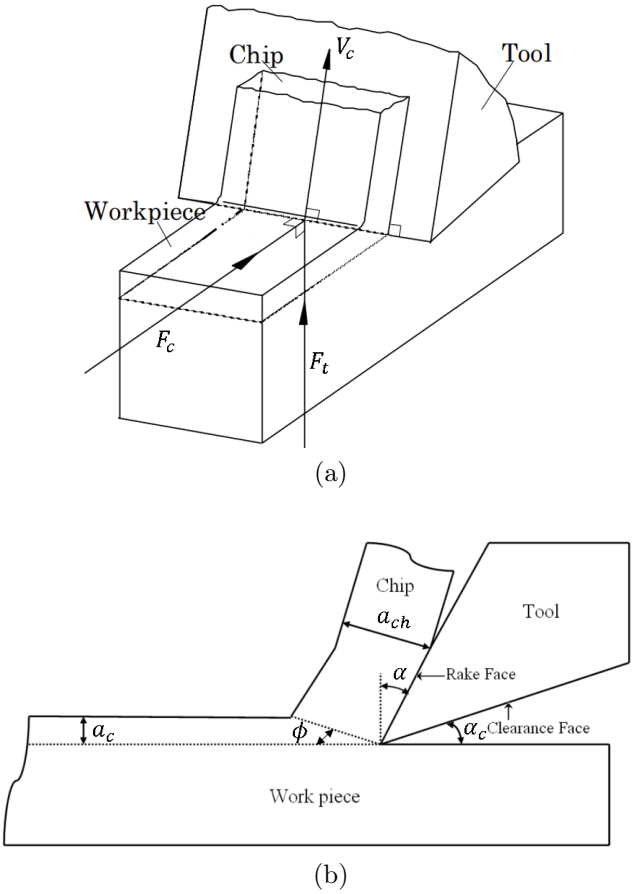

Figure 2.1: Schematic view of orthogonal metal cutting process.

or deformation zones. These plastic deformation zones have three main regions, as shown in Fig. 2.2 [1]. Chip formation takes place mainly in the primary shear zone (A-B) which extends from the tip of the tool to the junction between undeformed work material and the deformed chip. In high-speed machining, deformation occurs at the high strain rates, and when the tool moves through the workpiece material, the chip separates from the material and slides over the tool's rake face and forms secondary deformation zone (A-C) near tool rake face as shown in Fig. 2.2. Initially, the chip sticks to the tool's rake face and then slides over the tool and curls away. When the newly machined surface rubs with the flank of a tool, it creates a tertiary deformation zone (A-D).

The four types of chip produced can characterize the various cutting processes. In

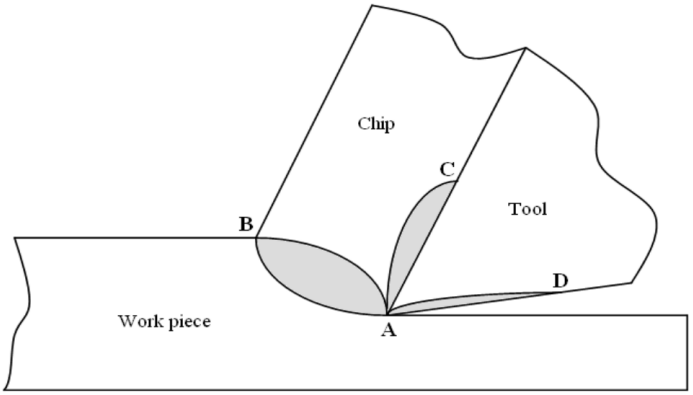

Figure 2.2: Deformation zones in metal cutting.

general, the chips are classified as continuous, continuous with a build-up-edge, serrated chips, and discontinuous chips as shown in Fig. 2.3 [3]. The continuous chip is produced when ductile materials like steel or aluminum are cut at high cutting speed. The continuous chip with build up edge (BUE) is produced due to high temperatures and high friction between tool and work-piece in low-speed machining of a ductile material. The semi-discontinuous chip forms in high-speed machining of harder machine materials like titanium and austenitic stainless steel. The discontinuous chip is observed when brittle materials like cast iron and brass are cut at low cutting speed.

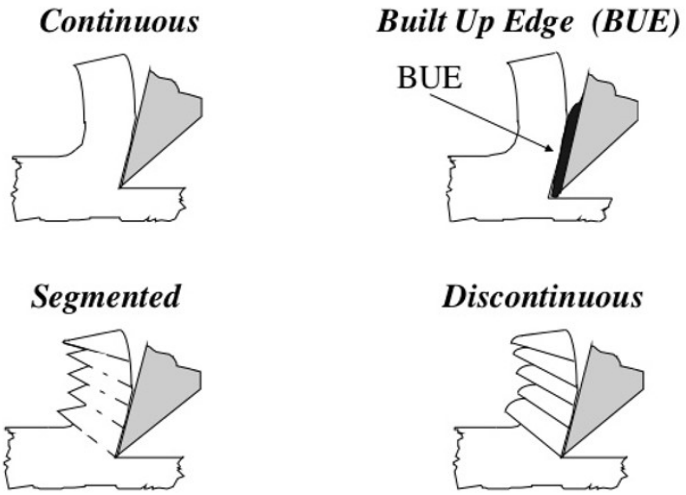

Figure 2.3: Continuous, continuous with BUE, segmented and discontinuous chips.

2.2 Chip Formulation

In orthogonal machining of the ductile material, the shear angle determines the efficiency of the process. A large value of shear angle indicates continuous chip and excellent surface finish while small value indicates discontinuous chip and low surface finish. So numerous researchers tried to develop a model for predicting the shear angle. In 1937, Piispanen [4] described shearing of the material as a deck of cards, moves inclined to the work-piece surface. In 1941, Merchant and Ernst [5] developed a theory to predict shear plane angle. Merchant's model assumes that the workpiece material deforms along a single thin shear plane. It also assumed a perfectly sharp tool, constant depth of cut, constant uncut chip thickness, constant relative velocity, and no contact along the flank. Ernst and Merchant [5] gave a relation between shear plane angle ϕ, rake angle α, and friction angle β as:

$$\phi = \frac{\pi}{4} - \frac{1}{2}(\beta - \alpha) \tag{2.1}$$

Later Merchant [6] used the minimum energy principle and found the same result as equation 2.1.

Slip-line field theory develops the relationship between stress and velocity in a shear plane. In this theory, material properties are assumed to be rigid and perfectly plastic. A slip-line is tangential all along its length to the direction of maximum shear stress. Combination of slip-lines in a plastic zone is called a slip line field. Lee and Shaffer [7] developed the first slip-line field model to describe the flow of the straight chip. All the slip-lines are straight in the Lee and Shaffer model because hydro-static pressure is constant all along the lines. Kudo [8] modified the straight slip-line to the curved slip-line which lead to rotating chips. Dewhurst [9] gave a relationship between chip curl and friction angle using slip-line theory and the relationship between the shear angle and friction angle can be given by:

$$\phi = \frac{\pi}{4} - (\alpha - \beta) \tag{2.2}$$

Oxley and Welsh [10] observed that chips form in a finite plastic zone and not in a simple shear line across a single shear plane. They introduced a parallel-sided shear zone model (thick shear zone model) representing slip-lines in the direction of the maximum shear stress and maximum shear strain. Okushima and Hitomi [11] also suggested a shear zone as a thick zone shear model. Although thick shear zone models were in good agreement with experimental data due to its complexity, it is difficult and cumbersome to use. So researchers started using the Finite Element Method to approximate the machining models. A first numerical approach for chip formation used a pre-define chip geometry and iterative solution by Usmi and Shirakashi [12]. The majority of earlier FE model for chip formations used a Lagrangian approach by Strenkowski [13], Lin and Lin [14] and Shih [15].

2.3 Constitutive Models

Flow stress is defined as the instantaneous value of stress needed to continuously deform material plastically. The relation of the flow stress with strain, strain-rate, and temperature together with some unknown constant is called as constitutive or flow stress model for the work material.

Oxley [16] developed predictive machining theory also know as Oxley's theory. This theory required thermal properties, flow stress data of the work material, cutting conditions, and tool geometry data to identify cutting forces, temperature, and stresses in orthogonal cutting. Oxley used power law as a constitutive model for the work material which is given by:

$$\sigma = \sigma_1 \varepsilon^n \tag{2.3}$$

where σ and ε are the effective flow stress and strain in the model. σ_1 and n are the stress and strain hardening coefficient respectively, and depend on the velocity modified temperature T_{mod}. Here T_{mod} can be calculated by considering the strain

rate and temperature effect on the material properties using the equation:

$$T_{\text{mod}} = T\left[1 - \nu log_{10}\left(\frac{\dot{\varepsilon}}{\dot{\varepsilon_0}}\right)\right]. \tag{2.4}$$

Here, T is the temperature at a point where material properties are required to be identify, ν is a material constant, $\dot{\varepsilon}$ is the strain rate, and $\dot{\varepsilon_0}$ is the reference strain rate.

Another unique constitutive model developed by Shirakashi [17] for capturing effects of loading history in metal cutting is defined by:

$$\sigma = B\left(\frac{\dot{\varepsilon}}{1000}\right)^M e^{aT}\left(\frac{\dot{\varepsilon}}{1000}\right)^m \left[\int_{strainpath}^{\frac{-aT}{N}} \left(\frac{\dot{\varepsilon}}{1000}\right)^{(-m/N)} d\varepsilon\right]^N \tag{2.5}$$

where a and m are constants and B, M and N are the functions of temperature. The integral part of the equation represents the history effect of strain and temperature for different strain rates. This model is challenging to implement in FEA softwares.

Based on a metal structure, Zerilli and Armstrong [18] developed a constitutive model for BCC and FCC materials. For BCC, constitutive model is written as:

$$\sigma = C_0 + C_1 exp(-C_3 T + C_4 ln\dot{\varepsilon}^*) + C_5 \varepsilon^n. \tag{2.6}$$

A constitutive model for FCC material is written as:

$$\sigma = C_0 + C_2 \bar{\varepsilon}^{1/2} exp(-C_3 T + C_4 ln\dot{\varepsilon}^*). \tag{2.7}$$

Here, T is absolute temperature, C_1-C_5 and n are material constants, and C_0 is the initial yield stress and depends on the solute and grain size. This model assumes that the relationship between flow stress and strain for BCC materials are not affected by temperature. However, for FCC materials, the relationship between flow stress and strain is strongly affected by temperature and strain rate. For steel (BCC material), the Zerilli-Amstrong model is accurate only up to 300 °C. For AA 6082 (FCC materials), this model gives inaccurate thermal softening and overestimated strain hardening. According to Jaspers et.al [19], the Johnson-Cook model is a better constitutive model for both the types of material.

The Johnson-Cook model is a widely used constitutive model given by equation 2.8. Ozel et al. [20] and Karpat et al. [21] used the Johnson-Cook constitutive equation to determine flow stress in the model. According to the Johnson-Cook model [22], the von Mises flow stress can be given by:

$$\bar{\sigma} = \left[A + B\bar{\varepsilon}^{n}\right]\left[1 + Cln\left(\frac{\dot{\bar{\varepsilon}}}{\dot{\bar{\varepsilon}}_0}\right)\right]\left[1 - \hat{T}^{m}\right] \tag{2.8}$$

where the non-dimensional temperature $\hat{T}$ is defined as:

$$\hat{T} = \begin{cases} 0 & \text{for } T < T_{\text{trans}} \\ \frac{T - T_{\text{trans}}}{T_{\text{melt}} - T_{\text{trans}}} & \text{for } T_{\text{trans}} \leq T \leq T_{\text{melt}} \\ 1 & \text{for } T > T_{\text{melt}} \end{cases} .$$

Here A, B, C, m, n are material constant and T_{melt} and T_{trans} are melting and transition temperature, respectively.

2.4 Friction models

The contact model near the tool-chip interface is the most significant part of FE simulations. It is essential to implement an accurate friction model for a reliable cutting simulation [20]. It affects the surface finish of the workpiece, chip morphology, cutting temperature, and tool wear [23]. Friction at the tool-chip interface is difficult to determine [24] due to the high strain and temperature occurring in a localized region. So initial research on FE modeling of the contact was ignored [25] or considered as a constant coefficient of friction based on Coulomb's law[26, 27]. Numerous researchers [28] used Zorev's model [29] in orthogonal cutting simulation; this model divides the cutting tool into sticking and sliding regions. High normal stress causing plastic deformation near the tool-chip interface region is defined as the sticking region, and relative low normal stress region next to the sticking region is defined as the slipping region. Friction at the tool-chip interface can be represented by normal and friction stress over the tool rake face. Ozel [20] considered five different contact models at the tool-tip interface in orthogonal machining using an updated Lagrangian

formulation and compared those results with the experiment results by Childs et al. [30]. The five contact models considered by Ozel are listed below:

1. Constant shear friction at the entire tool-chip interface:

   Constant shear friction was implemented at the entire tool-chip interface using Equation 2.9

   $$m = \frac{\tau}{k} \tag{2.9}$$

   here m is shear friction factor, k is shear flow stress of the workpiece at the tool-chip interface, and τ is maximum shear stress.

2. Constant shear friction in the sticking and Coulomb friction in the sliding region:

   In this approach, the tool-chip interface divides into a sticking region and a sliding region, l_p is the length of the sticking region, and l_c is contact length. The shear friction factor m is applied over the sticking region, and the coefficient of friction μ is applied over the sliding region.

3. Variable shear friction at the entire tool-chip interface:

   By modifying Equation 2.9, the empirical relation of the variable shear fraction at the entire tool-chip can be obtained.

   $$m = \frac{\tau_p}{k}\left[1 - exp\left\{ -\left(\frac{\sigma_n}{\tau_p}\right)^n \right\}\right]^{\frac{1}{n}} \tag{2.10}$$

   here n is a constant and τ_p is a limiting shear stress.

4. Variable friction coefficient at the entire tool-chip interface:

   By considering shear stress as a function of friction coefficient, variable friction coefficient along the tool can be defined as:

   $$\mu = \frac{\tau}{\sigma_n} \quad where, \quad \tau = f(\sigma_n) \tag{2.11}$$

5. Variable shear friction in the sticking region and variable friction coefficient in the sliding region:

This model used m from the third approach over the sticking region and μ from the forth approach over the sliding region.

Ozel identified that the error between experimental and FE simulation data is minimal when variable friction models at the entire tool-chip interface are used. Thus, the variable friction models should be used to obtain a more accurate result in the FE simulation of machining.

2.5 Finite Element Formulation

It is critical to select the appropriate finite element formulation for nonlinear dynamic problems. Three primary methods for formulation are listed below:

1. Lagrangian formulation
2. Eulerian formulation
3. ALE formulation

2.5.1 Lagrangian Formulation

Lagrangian nodes are coincident with the material so meshes, nodes, and elements move along with the material in the Lagrangian formulation. Boundary and interface nodes remain at the same node throughout the simulation. Fig. 2.4a shows the element mesh grid and material deformation when the Lagrangian formulation is used. In the deformed shape, mesh grids are still attached to the material and deformed with a material. The Lagrangian formulation is the most popular type of formulation in solid mechanics because it can evaluate the constitutive model at the same material point and produce history dependent data.

In this approach, as the tool cuts through the workpiece, chip and contact length are formed; therefore, the assumption of initial chip geometry is not required. However, when the element deforms, the mesh deforms with it and causes higher distortion issues in the model. Even with these limitations, the Lagrangian approach is still commonly used in by researchers [31] due to its ability to successfully model different

types of chip formulation [32, 33].

2.5.2 Eulerian Formulation

In the Eulerian formulation, nodes are coincident with spatial coordinates, and the material will flow through the mesh. Fig. 2.4b shows the element mesh grid and material deformation when an Eulerian formulation is used. In the deformed shape, the material will flow through the mesh grid, which is fixed spatially and causing no mesh distortion. In this approach, it is difficult to model boundary nodes because nodes will not remain at a specific material point. In an Eulerian formulation, material flows through the fixed mesh grid, causing no mesh distortion. Although this approach requires prior knowledge of the chip geometry and tool-chip contact length. Tay et al. [34] used the Eulerian approach for orthogonal machining modeling. This type of formation is useful for the Computational Fluid Dynamics (CFD) problem

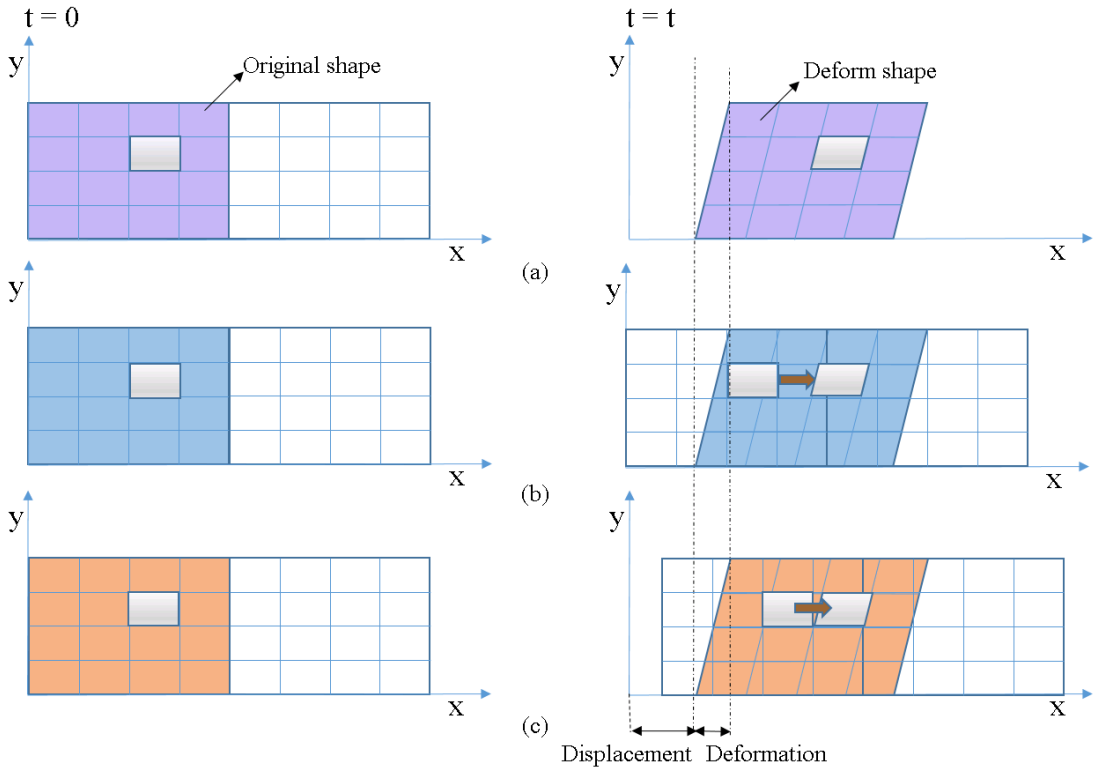

Figure 2.4: (a) Lagrangian (b) Eulerian and (c) ALE mesh in original and deform shape.

with high-velocity fluid where a specific spatial area is the main focus.

2.5.3 ALE Formulation

ALE is defined as Arbitrary Lagrangian-Eulerian formulation method. Both Lagrangian and Eulerian formulations have their benefits and disadvantage. ALE combines advantages of both the Lagrangian and Eulerian representation in a single formulation while minimizing the disadvantages. ALE uses Lagrangian nodes for boundary conditions and Eulerian nodes for internal nodes to overcome the excessive distortion in the primary and secondary shear zone. Fig. 2.4c shows an element mesh grid and material deformation when the ALE formulation is used. Although, this approach also requires prior knowledge of the chip geometry, chip-tool contact length and cannot model discontinuous chips.

In the Lagrangian approach, its simple to define a boundary, interface, and the contact condition also; the assumption of initial chip geometry is not required. Moreover, the drawbacks can be overcome by selecting appropriate chip separation criteria, and mesh distortion can be controlled by the hourglass method. So due to those advantages, the Lagrangian formulation is considered in this study.

2.6 Chip Separation Criteria

Numerous researchers [25, 30, 35] used the Eulerian approach to formulate chip in orthogonal metal cutting, which requires fewer elements and less computational time. However, it requires prior knowledge of the chip geometry and tool-chip contact length. So many researchers [12, 13, 14, 15] inclined to use the Lagrangian approach in the orthogonal cutting model, which allows the chip to be modeled from incipient stage to steady stage without any prior assumption of chip morphology. Since this method requires chip separation criteria of the chip from the workpiece material, realistic separation criteria have been an essential factor in this approach of FE modeling.

Usui et al. [12] used geometrical criteria based on node separation when the tool node is sufficiently close to the workpiece node, one node from the predefined parting line moves to the rake face and other node remains on the machined surface. Zhang et al. [36] and Shih [15] also used distance-based criteria, in this the value of critical length at which node split was crucial to identify. Carroll et al. [37] and Xie et al. [38] used effective plastic strain as a separation criterion. They used the value in the range of 0.4 to 1.5. Lin et al. [14] observed that the effective plastic strain depends on the cutting parameters, e.g. uncut chip thickness and tool rake angle. Iwata et al. [39] considered stress-based ductile fracture criteria for chip formulation. However, Chen et al. [40] pointed out that the separation criteria should not be considered as a numerical value and treated as a material constant, which can be measured experimentally.

Despite the criteria used as the tool advances, a predefined parting line of the nodes is required for all these chip separation criteria. That is not realistic because in actual machining material does not separate in a straight path. Also, it is not certain that the simulation will follow a predefined path in the influence of high deformation.

Shaw [41] was first to consider that the chip separation criteria in the formation of the new surface in machining requires energy on the order of J/m^2 which is negligible in cutting compared to plastic and friction forces. Later, Atkins [42] showed that the chip separation criteria is in range of KJ/m^2 rather than J/m^2, and it is crucial to consider the energy required to generate new surface in machining analysis.

2.7 Thermal Modelling

In machining, most of the plastic work converts into the heat. This heat is a significant source of temperature rise in a chip. Determining temperature in the tool, chip, and the workpiece is essential since it has a considerable influence on the tool wear, chip morphology, surface finish, and cutting forces. Deformation in the primary shear zone and friction between tool-chip interface are the main cause for the higher chip

temperature. Q_1 is a heat source in a primary shear zone, which profoundly affects flow stress and tool temperature. Q_2 is a heat source at the secondary deformation zone at the tool-chip interface. The maximum temperature occurs at this zone which causes tool wear, and Q_3 is a heat source at the tertiary deformation zone.

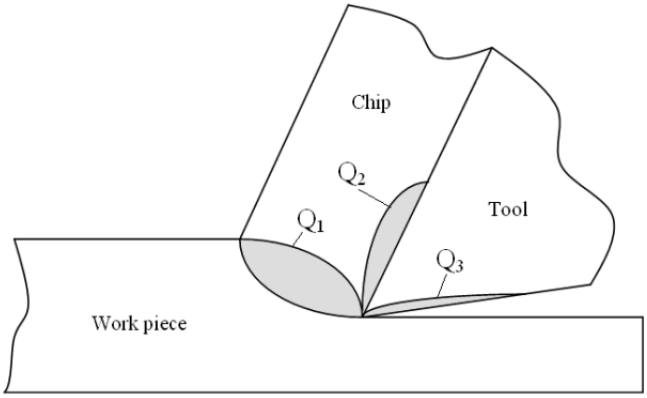

Figure 2.5: Heat source location in orthogonal metal cutting [1].

Inelastic heat fraction or Taylor and Quinney coefficient [43] is an essential factor to consider for numerical simulation of transient problems. The ratio of generated heat to plastic work is known as inelastic heat fraction. Dissipation of plastic work depends on the strain, strain rate, and temperature. It typically assumes between 0.8 to 1 [44] and for steel is it usually considered as 0.9 [45, 46].

In previous research, only friction behavior between the tool-chip interface has been considered while thermal interaction between the tool-chip interface has been neglected. However, in high-speed machining thermal contact between tool and chip is required to prescribe for simulating tool temperature.

For the workpiece material 1045 steel and uncoated WC tool Yen et al. [47] used a value of 100 KW/m^2 °C for the heat transfer coefficient (h) at the tool-chip interface. Klocke et al. [48] used 1045 steel workpiece and SiC-ceramic tool and assumed a very high value of the heat transfer coefficient, which depended on the experimental result of temperature and chip surface in the secondary shear zone. Ozel [20] used 100 KW/m^2 °C for h at tool-chip interface for the same material used by Yen et al. [47].

Xie et al. [49] used value 10 KW/m^2 °C for h at the tool-chip interface for 1045 steel workpiece and an uncoated WC tool. Then Iqbal et al. [50] applied a different heat transfer coefficient to calculate the interface temperature and compared those results with the experimental data which lead to a conclusion that the range of h for 1045 steel workpiece and uncoated cemented carbide tool lies between 100-300 KW/m^2 °C for different cutting speeds.

CHAPTER 3: FINITE ELEMENT MODEL

3.1 Johnson-Cook Constitutive Model

In machining, hardening occurs due to high strain and strain rates, moreover thermal softening occurs due to high temperature so for simulating material behavior, an accurate flow stress model is required. The flow stress model proposed by Johnson and Cook [22] is suitable for modeling problems that include high strain, high strain rate, strain hardening, and non-linearity. The Johnson-Cook model is one of the most accurate model for describing material behavior and chip formation in machining [51]. This model is a strain-rate and temperature dependent visco-plastic material model suitable for large strain range of 10^2 to 10^6 s^{-1}. This model is given by Equation 3.1 as:

$$\bar{\sigma} = \left[A + B(\bar{\varepsilon}^{pl})^n\right]\left[1 + C\ln\left(\frac{\dot{\bar{\varepsilon}}^{pl}}{\dot{\varepsilon}_0}\right)\right]\left[1 - \hat{T}^m\right] \tag{3.1}$$

Where the non-dimensional temperature $\hat{T}$ is defined as:

$$\hat{T} = \begin{cases} 0 & \text{for } T < T_{\text{trans}} \\ \frac{T - T_{\text{trans}}}{T_{\text{melt}} - T_{\text{trans}}} & \text{for } T_{\text{trans}} \leq T \leq T_{\text{melt}} \\ 1 & \text{for } T > T_{\text{melt}} \end{cases} .$$

In Equation 3.1, the first term in for isotropic hardening, the second term accounts for strain rate hardening, and the third term accounts for thermal softening. Where $\bar{\sigma}$ is the equivalent stress, $\bar{\varepsilon}^{pl}$ is the equivalent plastic strain, $\dot{\bar{\varepsilon}}^{pl}$ is the plastic strain rate, $\dot{\varepsilon_0}$ is the reference strain rate, T_{trans} is the transition temperature, and T_{melt} is the melting temperature. A is the initial yield stress, B is the hardening modulus, n is the work-hardening exponent, C is the strain rate dependency coefficient, and m is the thermal softening coefficient. These constants can be identified through the

Table 3.1: Johnson-Cook constants for AISI 1045 steel

A (MPa)	B (MPa)	n	m	C	$T_{\text{melt}}(^{\circ}\text{C})$	$T_{\text{trans}}(^{\circ}\text{C})$	$\dot{\varepsilon}_0$ (s^{-1})
615.8	667.6	0.255	1.078	0.0134	1460	25	1

high strain rate deformation test using Split-Hopkinson pressure bar (SHPB), and the values are adopted from [52]. These constants for AISI 1045 steel are given in Table 3.1.

Thermal softening and strain rate hardening can be identified from the figures below. Fig 3.1 to Fig.3.4 shows stress-strain response of AISI 1045 steel at different strain rates at fixed temperatures. As temperature increases equivalent stress trends decreases for various strain rate due to the effect of thermal softening in material. Fig 3.5 to Fig. 3.8 shows stress-strain responses of AISI 1045 steel at different temperatures at fixed strain rates.

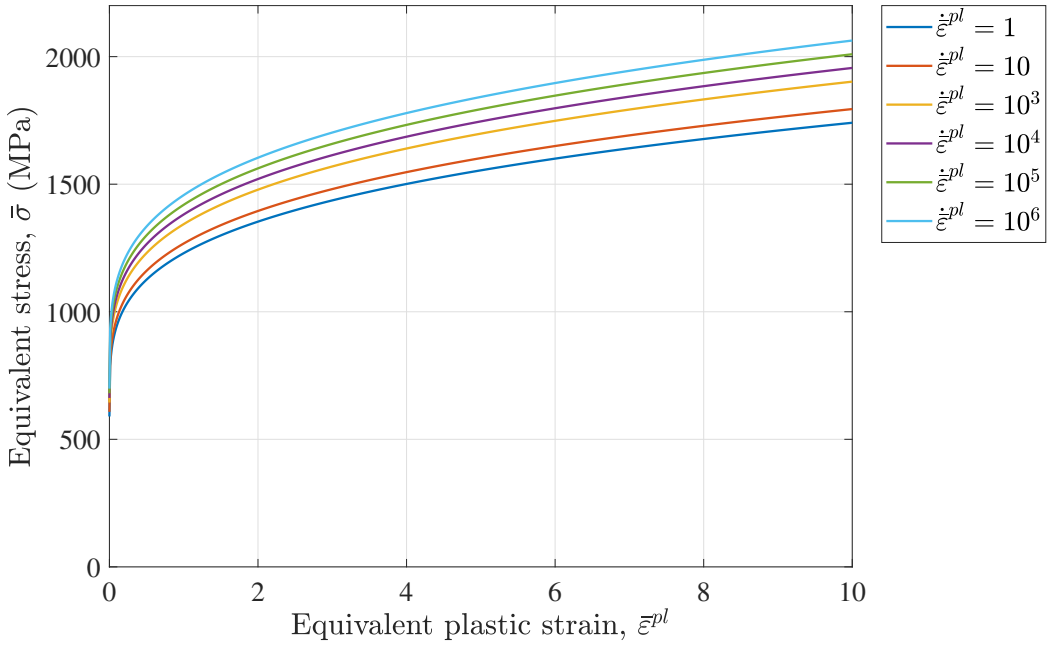

Figure 3.1: $\bar{\sigma}$ vs $\bar{\varepsilon}^{pl}$ for AISI 1045 steel at various strain rates ($\dot{\bar{\varepsilon}}^{pl}$) and at a fixed temperature T = 100°C.

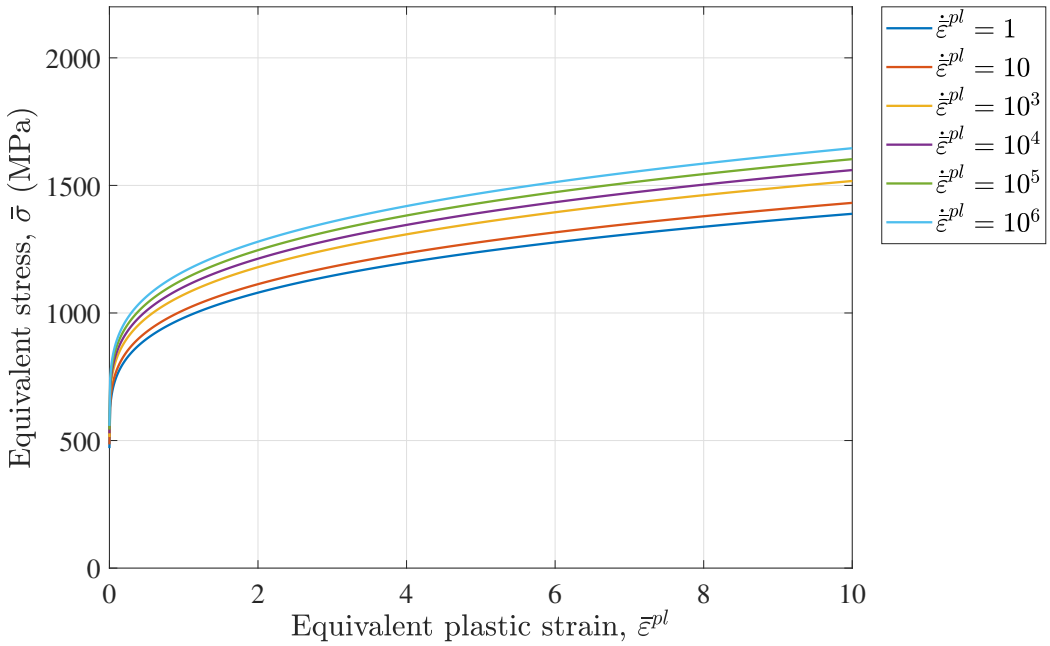

Figure 3.2: $\bar{\sigma}$ vs $\bar{\varepsilon}^{pl}$ for AISI 1045 steel at various strain rates ($\dot{\bar{\varepsilon}}^{pl}$) and fixed temperature T = 400°C.

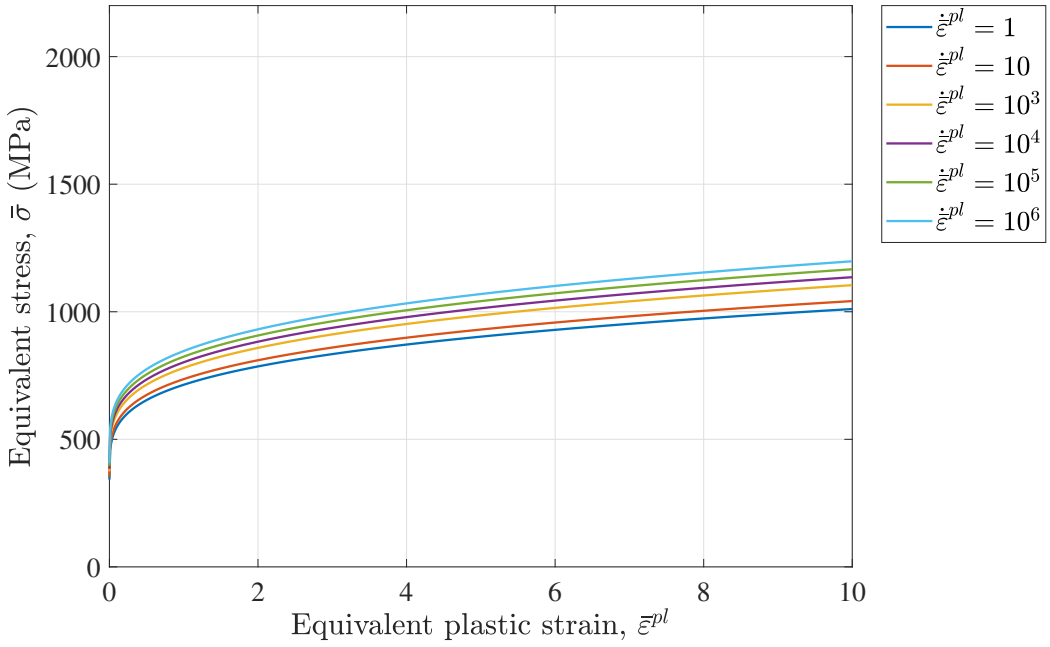

Figure 3.3: $\bar{\sigma}$ vs $\bar{\varepsilon}^{pl}$ for AISI 1045 steel at various strain rates ($\dot{\bar{\varepsilon}}^{pl}$) and fixed temperature T = 700°C.

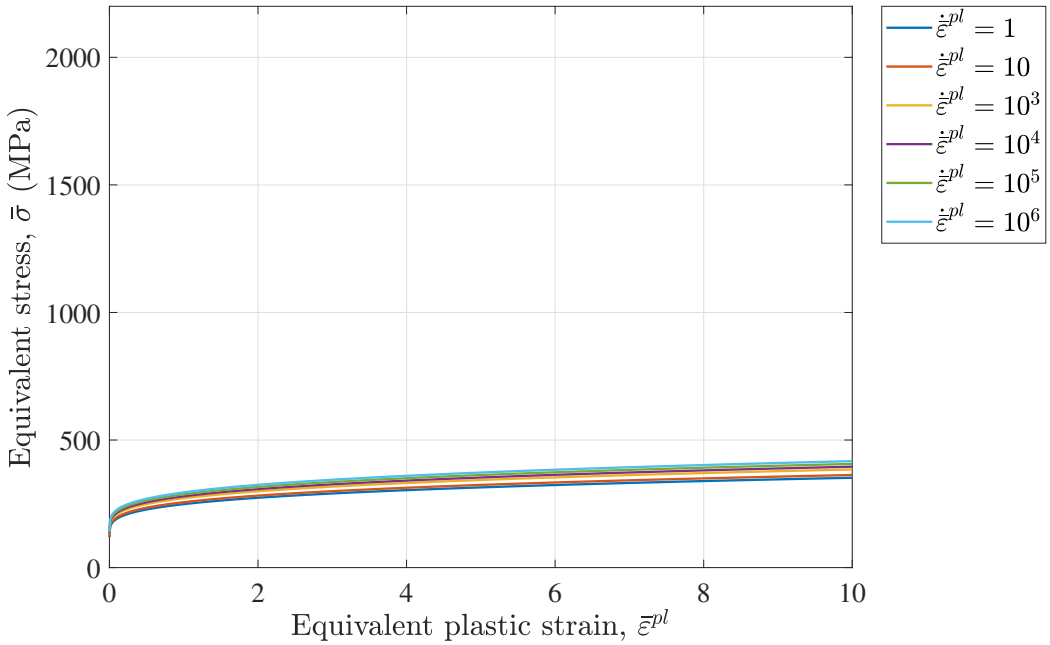

Figure 3.4: $\bar{\sigma}$ vs $\bar{\varepsilon}^{pl}$ for AISI 1045 steel at various strain rates ($\dot{\bar{\varepsilon}}^{pl}$) and fixed temperature T = 1000°C.

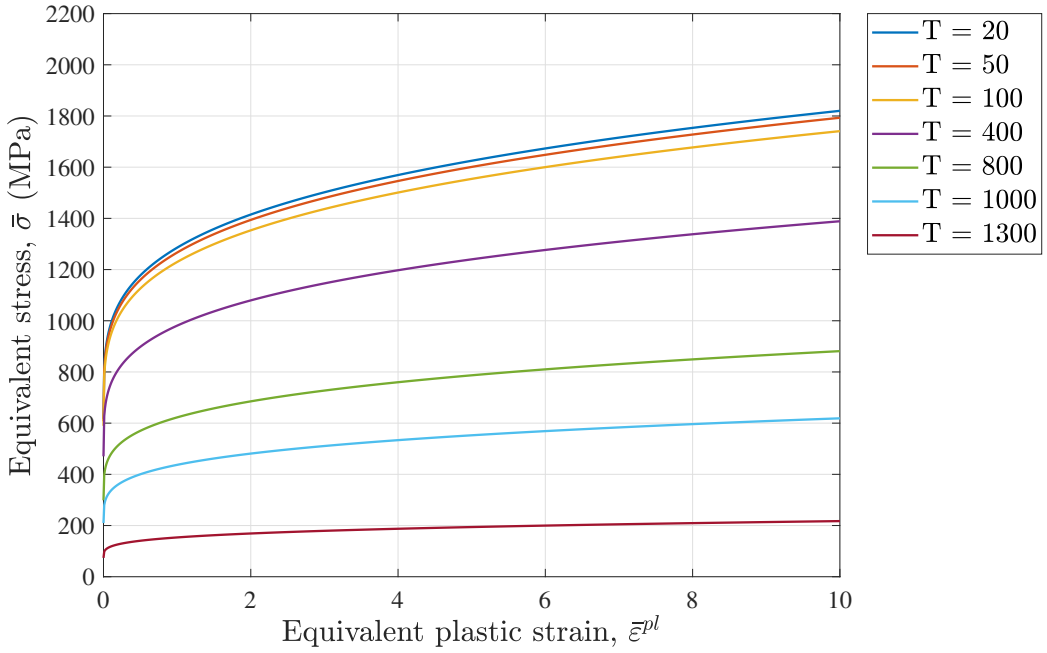

Figure 3.5: $\bar{\sigma}$ vs $\bar{\varepsilon}^{pl}$ for AISI 1045 steel at various temperatures (°C) and at a fixed strain rate $(\dot{\bar{\varepsilon}}^{pl}) = 1$.

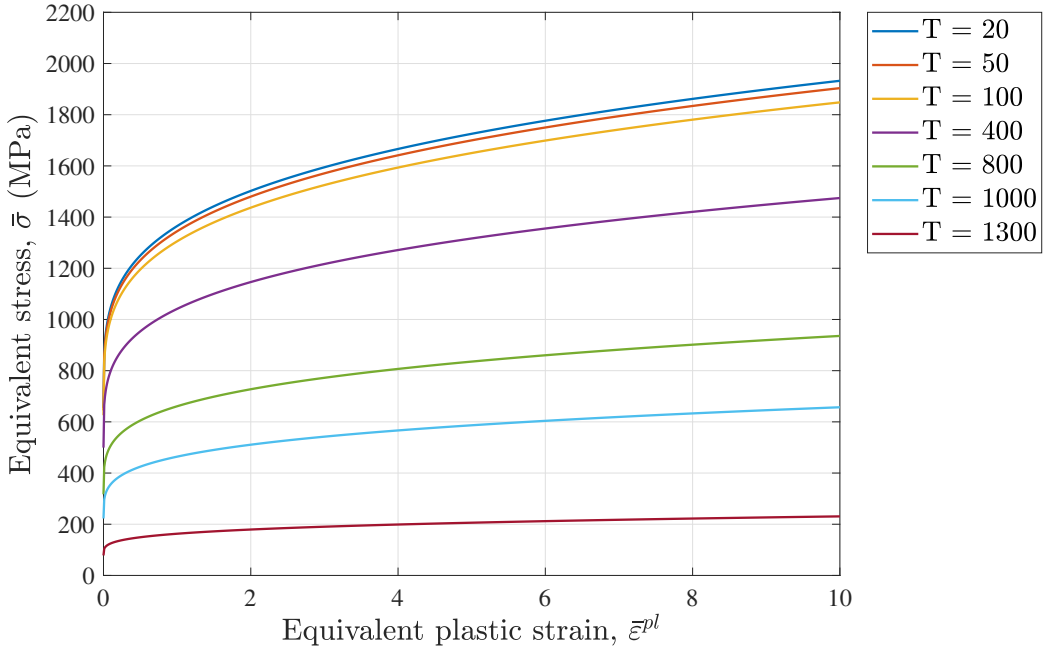

Figure 3.6: $\bar{\sigma}$ vs $\bar{\varepsilon}^{pl}$ for AISI 1045 steel at various temperatures (°C) and fixed strain rates $(\dot{\bar{\varepsilon}}^{pl}) = 100$.

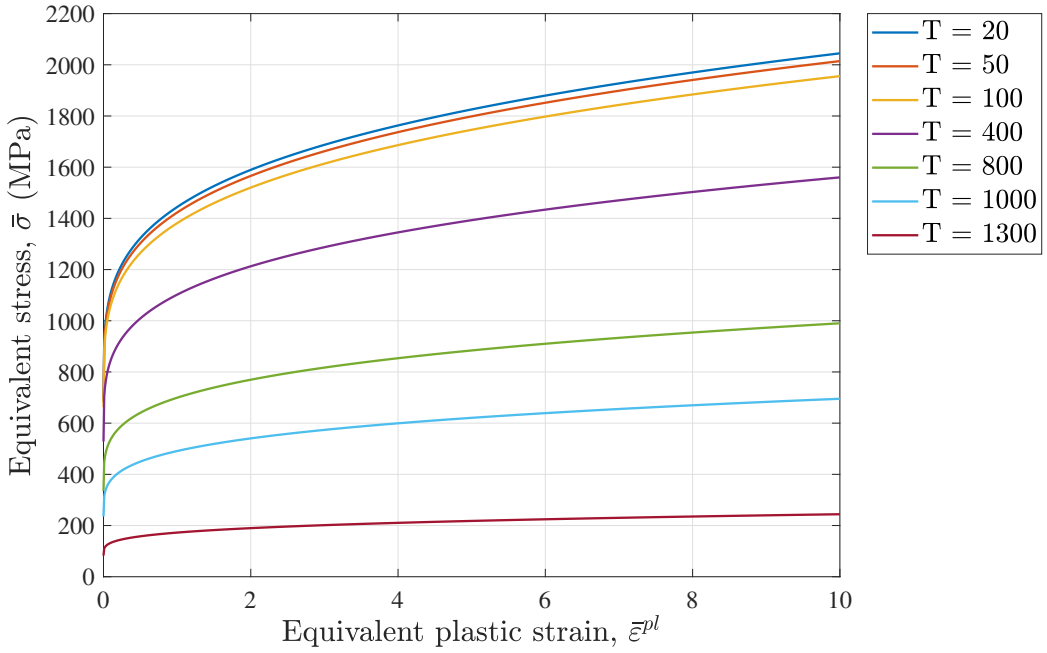

Figure 3.7: $\bar{\sigma}$ vs $\bar{\varepsilon}^{pl}$ for AISI 1045 steel at various temperatures (°C) and fixed strain rates $(\dot{\bar{\varepsilon}}^{pl}) = 10^3$.

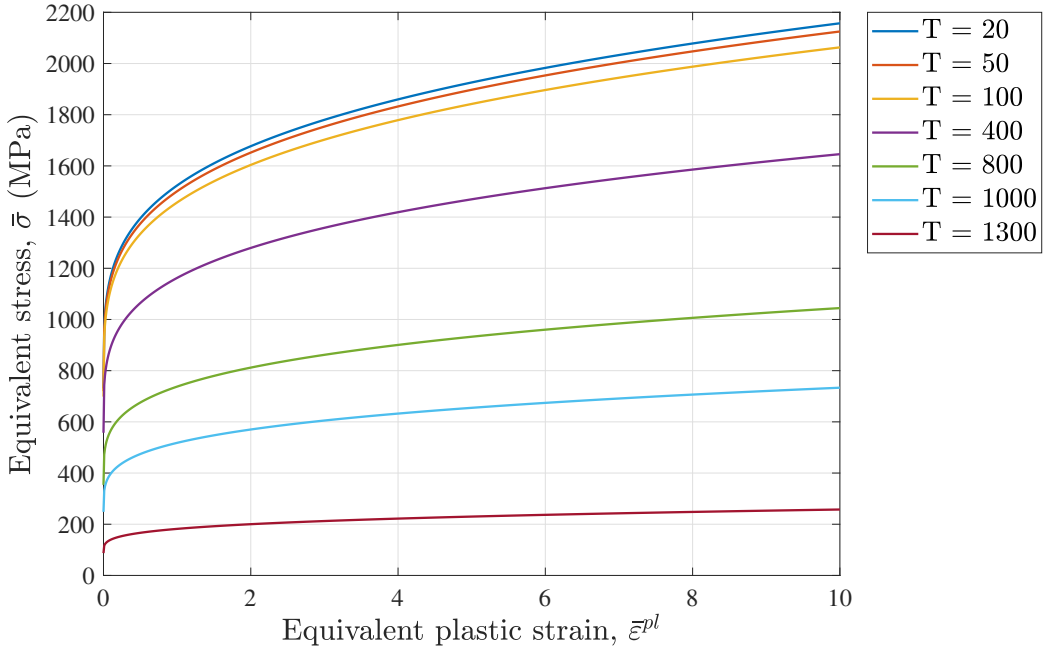

Figure 3.8: $\bar{\sigma}$ vs $\bar{\varepsilon}^{pl}$ for AISI 1045 steel at various temperatures (°C) and fixed strain rates $(\dot{\bar{\varepsilon}}^{pl}) = 10^5$.

3.2 Johnson-Cook Damage Model

To model the chip formulation and chip separation, a fracture-based model was used. Damage initiation and evaluation were considered for modeling of the damage. The Johnson-Cook damage model [53] was used with the Johnson-Cook plasticity model in this study. This model was divided into two main parts: Damage initiation and Damage evolution.

3.2.1 Damage Initiation

The Johnson-Cook damage model is based on the value of the equivalent plastic strain, and damage initialization is assumed to occur when the damage parameter (ω) exceeds one. The damage parameter follows cumulative damage law and is define (ω) as:

$$\omega = \sum \left(\frac{\Delta \bar{\varepsilon}^{pl}}{\bar{\varepsilon}_f^{pl}} \right) \tag{3.2}$$

$\Delta \bar{\varepsilon}^{pl}$ and $\bar{\varepsilon}_f^{pl}$ are an increment of the equivalent plastic strain and failure strain, respectively. The failure strain $\bar{\varepsilon}_f^{pl}$ can be defined as:

$$\bar{\varepsilon}_f^{pl} = \left[d_1 + d_2 exp\left(d_3 \frac{p}{q} \right) \right] \left[1 + d_4 \ln\left(\frac{\dot{\bar{\varepsilon}}^{pl}}{\dot{\varepsilon}_0} \right) \right] \left(1 + d_5 \hat{T} \right) \tag{3.3}$$

Where the non-dimensional temperature $\hat{T}$ is defined as:

$$\hat{T} = \begin{cases} 0 & \text{for } T < T_{\text{trans}} \\ \frac{T - T_{\text{trans}}}{T_{\text{melt}} - T_{\text{trans}}} & \text{for } T_{\text{trans}} \leq T \leq T_{\text{melt}} \\ 1 & \text{for } T > T_{\text{melt}} \end{cases} .$$

Where d_1 is an initial failure strain, d_2 is an exponential factor, d_3 is a triaxiality factor, d_4 is a strain rate factor, and d_5 is a temperature factor. T_{melt} and T_{trans} are melting and reference temperatures, respectively. Here, d_3 needs to be considered positive because Abaqus has a difference in sign for parameter d_3 in the expression of $\Delta \bar{\varepsilon}^{pl}$ from the original equation [53]. Identifying the value of these five damage parameters involves a series of experimental fracture tests that vary the stress tri-

Table 3.2: Johnson-Cook damage parameters for AISI 1045 steel

Set	d_1	d_2	d_3	d_4	d_5
I	0.04	1.03	1.39	0.002	0.46
II	0.05	4.42	2.73	0.0018	0.55

axiality, strain-rate, and temperature. In this study, we are considering two sets of damage parameters, and the values are adopted from [52] and [54], respectively. The damage constants of AISI 1045 steel is presented in Table 3.2.

3.2.2 Damage Evolution

After damage initiation in ductile material, the regular stress-strain relationship graph is not able to represent accurate material behavior [55]. The model become mesh dependent after damage initiation, so to reduce this mesh dependency, Hillerborg's model [56] is used to create a mesh independent model. Fig. 3.9 shows the stress-strain relationship of a material undergoing damage. Line a-b shows linear elastic behavior of the ductile material, b-c shows plastic yielding with strain hardening, point c identifies the damage initiation point, and d is fracture point. C-d curves follow damage evolution law of the stiffness degradation in the region of strain localization, and c-d' shows ductile material's behavior in the absence of damage. σ_y^0 and $\bar{\varepsilon}_f^{pl}$ are yield stress and equivalent plastic strain, respectively. $\bar{\varepsilon}_f^{pl}$ is the equivalent plastic strain at failure when D reaches one at point d. At point c, when $\omega = 1$, damage initiated starts from D = 0 and it evolve over line c-d and at point d it is reaches to the value one.

Hillerborg defines the energy required to open a unit area of the crack, G_f, as a material parameter. In this approach softening response after damage initiation is defined by a stress-displacement response rather than a stress-strain response. Fracture energy is given as:

$$G_f = \int_{\bar{\varepsilon}_0^{pl}}^{\bar{\varepsilon}_f^{pl}} L\bar{\sigma}_y d\bar{\varepsilon}^{pl} = \int_0^{\bar{u}_f^{pl}} \bar{\sigma}_y d\bar{u}^{pl} \tag{3.4}$$

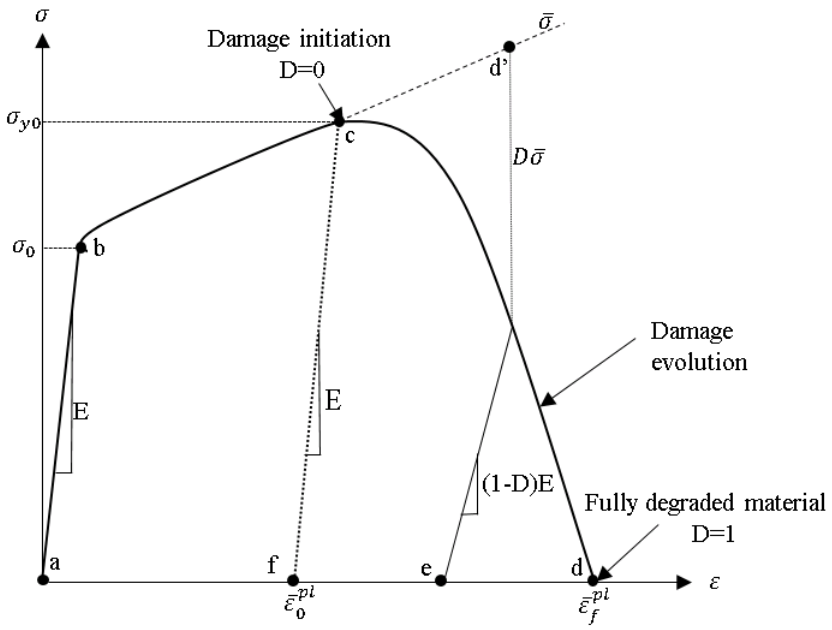

Figure 3.9: Stress-strain curve after damage.

Here, $\bar{u}^{pl}$ is equivalent plastic displacement, and L is characteristic length based on the element geometry. L is assumed to be the square root of the integration point element area. The damage evolution law can be specified in terms of $\bar{u}^{pl}$ or G_f. Both the options take into account the characteristic length of the element to alleviate mesh dependency results. Once the damage initiation criterion has been reached, the effective plastic displacement, $\bar{u}^{pl}$, is defined as:

$$\dot{\bar{u}}^{pl} = L\dot{\bar{\varepsilon}}^{pl} \tag{3.5}$$

Evolution of damage variable with relative plastic displacement can be defined as linear or exponential form.

3.2.2.1 Linear Damage Evolution

Crack propagation occurs when the energy release rate is equal to or higher than critical energy rate, G_f. For linear damage, evolution law is defined as:

$$G_f = \frac{1}{2}\bar{u}_f\bar{\sigma}_d \tag{3.6}$$

A scalar stiffness degradation variable (SDEG) D is used in Abaqus to quantify the damage evolution based on increment of equivalent plastic displacement. Once the damage initiation criteria is met the linear damage parameters increases according to:

$$D = \frac{L\dot{\bar{\varepsilon}}^{pl}}{\bar{u}^{pl}} = \frac{\dot{\bar{u}}^{pl}}{\bar{u}_f^{pl}} \tag{3.7}$$

where,

$$\bar{u}_f^{pl} = \frac{2G_f}{\sigma_{y0}}$$

This formulation of the model ensures that the energy dissipated during the damage evolution process is G_f. When D = 1 in an element, the element is removed from the model. In Figs. 3.10a and 3.11a areas under the curve $\sigma(\bar{u})$ represent G_f.

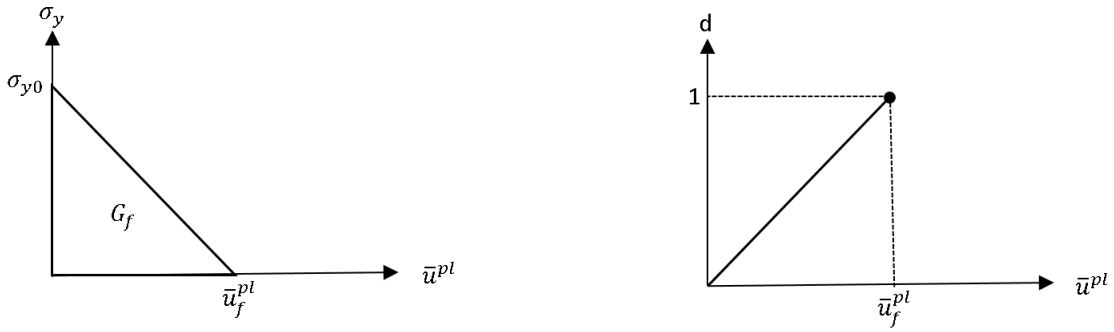

(a) (b)

Figure 3.10: (a) Flow stress vs Equivalent plastic displacement (b) Damage parameter vs Equivalent plastic displacement in linear damage model.

3.2.2.2 Exponential Damage Evolution

Critical energy release rate, G_f, for exponential damage evolution is defined as:

$$G_f = \int_0^{\bar{u}_f^{pl}} \bar{\sigma}_y d\bar{u} \tag{3.8}$$

Once the damage initiation criteria is met the Exponential damage parameters increases according to:

$$D = 1 - exp\left(- \int_0^{\bar{u}_f^{pl}} \frac{\bar{\sigma}_y}{G_f} du \right) \tag{3.9}$$

This formulation of the model ensures that the energy dissipated during the damage evolution process is $0.99G_f$ because damage parameter practically cannot reach the value one for exponential evolution.

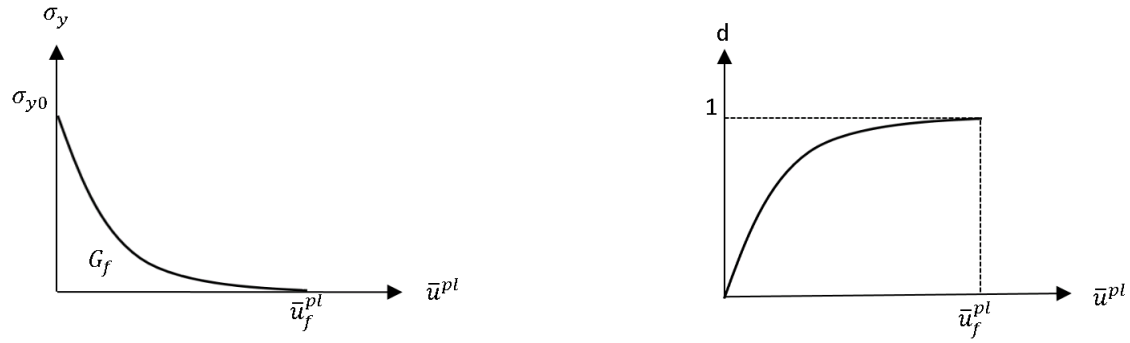

(a) (b)

Figure 3.11: (a) Flow stress vs Equivalent plastic displacement (b) Damage parameter vs Equivalent plastic displacement in exponential damage model.

3.3 Selection of Critical Energy Release Rate

In this study, critical energy release rate (G_f) is used as a chip separation criterion. Irwin was one of the first to study the behavior of the crack [57]. He considered three different types of the fracture mode in Linear Elastic Fracture Mechanics (LEFM): mode I, mode II, and mode III.

1. Mode I:

   The forces are perpendicular to the crack and pulled the crack open. This is mentioned as an opening mode.

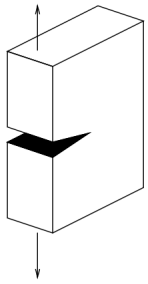

Mode I

2. Mode II:

   The forces are parallel to the crack, where one force pushes the top half of the crack back, and other force pulls the bottom part of crack forward. This mode is mentioned as the in-plane shear mode, and it causes shear crack along the plane.

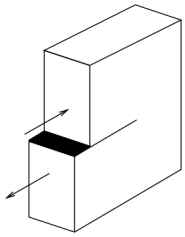

Mode II

The orthogonal cutting process can be described using mode I and mode II of fracture mechanics, as shown in Fig. 3.12 [58]. Opening mode (mode I) can relate to the top figure of the portion highlighted in Fig. 3.13, and in-plane shear mode (mode II) can refer to the bottom figure of the part highlighted in Fig.3.13.

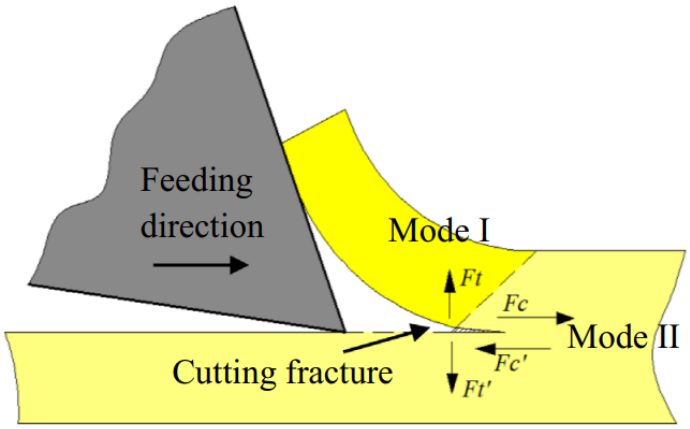

Figure 3.12: Fracture modes in orthogonal cutting model [2].

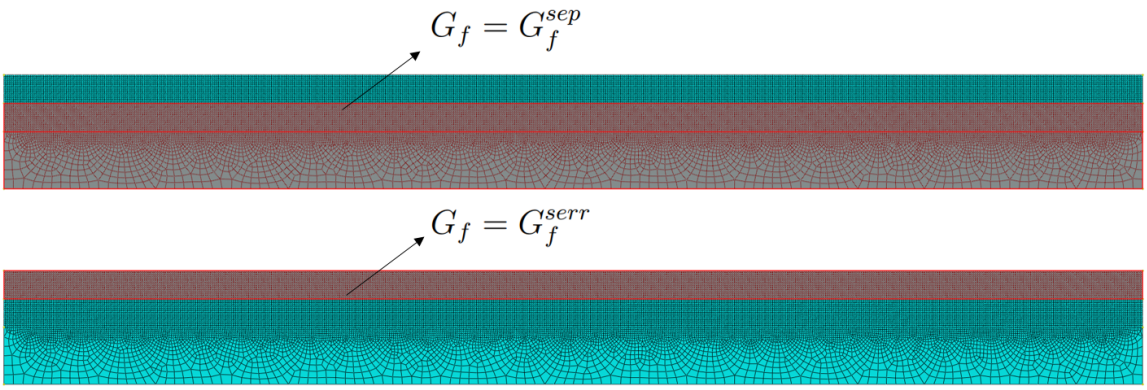

Figure 3.13: Energy spent to form new surface when chip generates, $G_{\mathrm{f}}^{\mathrm{sep}}$, Energy spent in forming new surface for chip serration, $G_{\mathrm{f}}^{\mathrm{serr}}$.

For isotropic linear elastic material fracture toughness, G_{f} can be defined as:

$$G_{\mathrm{f}}^{(\mathrm{sep,serr})} = \frac{1-\nu^2}{E}\mathrm{K}_{\mathrm{Ic,IIc}}^2, \quad \text{for plane strain} \tag{3.10}$$

Here, $\mathrm{K_c}$ is the stress intensity factor and the subscript I and II indicate the crack opening modes. Value of $\mathrm{K_c}$ is adopted from [59] and listed in Table 3.3. Critical energy release rate for chip separation and chip serration is shown as, $G_{\mathrm{f}}^{\mathrm{sep}}$ and $G_{\mathrm{f}}^{\mathrm{serr}}$, respectively. Necessary condition for crack growth in terms of toughness is that the $G_{\mathrm{f}}^{\mathrm{sep}}$ should be greater than $G_{\mathrm{f}}^{\mathrm{serr}}$ [60]. Linear damage model for $G_{\mathrm{f}}^{\mathrm{sep}}$ and exponential damage model for $G_{\mathrm{f}}^{\mathrm{serr}}$ are selected by conducting parametric studies.

Table 3.3: Fracture toughness properties of AISI 1045 steel

K_{Ic} ($MPa\sqrt{m}$)	K_{IIc} ($MPa\sqrt{m}$)	G_f^{sep} (J/m^2)	G_f^{serr} (J/m^2)
55.4	71.5	14000	24000

3.4 Friction Modeling

Friction along with the tool-chip interface during the cutting process is a very complex aspect in machining. It can influence the chip morphology, cutting temperature, tool wear, and normal stress between tool and workpiece, so the accuracy of the predicted result highly depends on the choice of friction model. Therefore, it is necessary to understand the friction phenomena across the tool to develop an accurate model for predicting cutting force and temperature.

According to Zorev [29], the normal stress is greatest at the tool tip and gradually decreases to zero at the point where the chip separates from the rake face. As shown in Fig. 3.14 sticking region occurs near the cutting edge of the tool-chip interface, and the friction shear stress τ is equal to average shear flow stress at the tool-chip interface, τ_p. Sliding friction occurs at the remainder of the tool-chip interface area, and the friction shear stress is calculated using the coefficient of friction, μ. Normal and shear stresses for both regions can be defined as:

1) For the sticking region:

$$\tau_f(x) = \tau_p \quad when \quad \mu\sigma_n(x) \geq \tau_p, \quad 0 < x \leq l_p \tag{3.11}$$

2) For the sliding region:

$$\tau_f(x) = \mu\sigma_n(x) \quad when \quad \mu\sigma_n(x) < \tau_p, \quad l_p < x \leq l_c \tag{3.12}$$

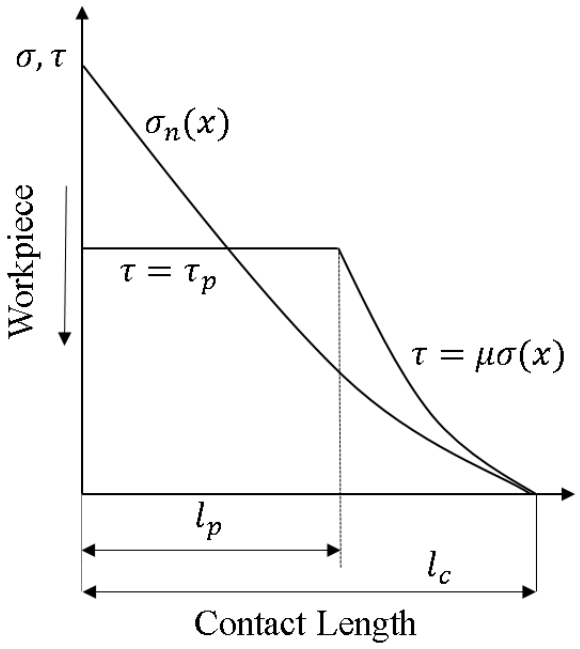

Figure 3.14: Normal and friction shear stress distribution along the tool rake face.

Zorev's model has been used in numerous literature, but it considered constant friction coefficient and independent to normal stress in a slip zone and has been criticized by the prior researchers [61, 62]. So stress based friction model proposed by Yang and Liu [63] is used in slip zone for this study. Using the split tool technique for normal and shear stress distribution, experimental data for AISI 1045 steel is adopted from [64], and is plotted in Fig. 3.15 over the entire rake face length of the tool. Friction model is plotted in Fig. 3.16, and limiting shear stress, τ_{p}, is considered as 535 MPa. Friction shear stress for slip zone can be given by:

$$\tau_f(\sigma_n) = -7.31e-9\sigma_n^4 + 2.52e-5\sigma_n^3 - 0.011\sigma_n^2 + 3.6218\sigma_n - 2.02 \tag{3.13}$$

The tool-chip contact in Abaqus is modeled as penalty stiffness contact formulation where tool and workpiece are defined as slave and master surfaces, respectively.

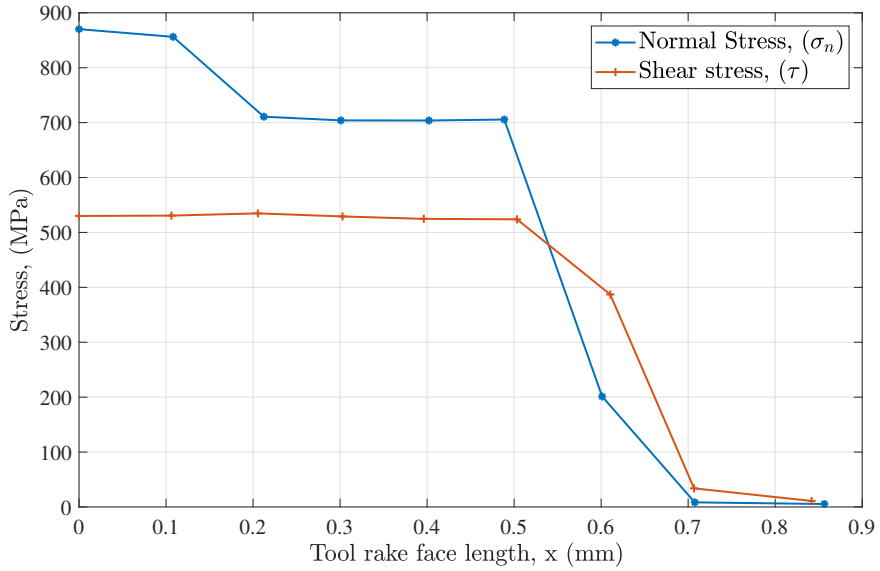

Figure 3.15: Shear and normal stress distribution over tool rake face.

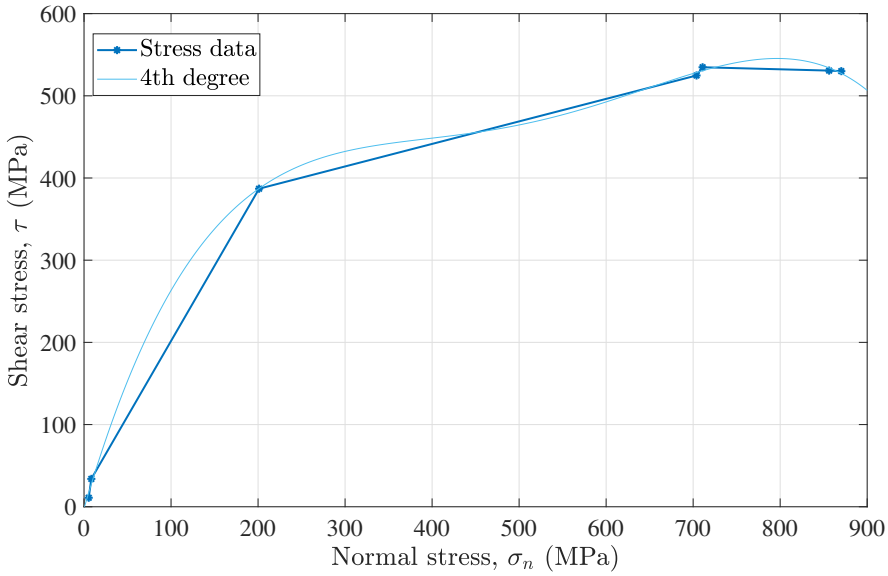

Figure 3.16: Stress based friction model in slipping zone.

3.5 Thermal Modelling

In a metal cutting, a significant amount of work is dissipated due to plastic deformation and friction. Most of the dissipated work is converted into the heat and raises the tool and workpiece temperature. To study the temperature fields in the tool and

the chip, accurate thermal behavior at the tool-chip interface is essential to model. In this study, thermal gap conduction between workpiece and tool is considered 100 KW/m^2 °C [50].

CHAPTER 4: FEM FORMULATION IN ABAQUS

4.1 Finite Element Method

Due to the advancement in the computer software and hardware, solving mathematical problems with computer codes became more a suitable approach for researchers. Many assumptions in the analytic model lead nonphysical solutions for some problems. So newer software like Abaqus/Standard, Abaqus/ Explicit, ANSYS, LS-DYNA, Advantedge, Deform 2D/3D helped to implement this mathematical idea into the software.

Finite Element Method (FEM) is a numerical method to find an approximate solution for engineering problems. FEM discretize parts into a finite number of elements (mesh) and solve constitutive models for the individual element. Mesh of the part should be small enough to get a good result and large enough to reduce computational time. FEM uses shape functions to interpolate the solution of the entire part from the value obtained at the integration nodes. Gaussian-quadrature is the most popular shape function due to its ability to accurately integrate polynomials of large degrees. Strong form is a higher order governing differential equation of any given problem. Three primary methods to convert the strong form to the weak form includes a direct, variation, and weighted residual method (WRM). The galerkin approach in the WRM method is a widely used technique due its simplicity and adaptability. Using a weak form of the constitutive model, a set of algebraic system equations can construct individual stiffness and force matrices. Combining these individual matrices with the process of superposition creates a global matrix. Boundary conditions are imposed on this global matrix and multiple methods are utilized to solve the system of equation within the global matrix. For a small system, direct methods like Gauss

elimination, LU decomposition, and Cholesky decomposition are used. For dynamic and time-dependent problems, explicit and implicit methods are used. For this study, we are using an explicit approach to solve the system of equations.

4.2 Finite Element Modeling

As discussed earlier, an Updated Lagrangian finite element formulation is used in this study. Discussed governing equation and solution methods are adopted form Belytschkoi et al. [65]. Strong form of balance of linear momentum is defined as:

$$\frac{\partial \sigma_{ji}}{\partial x_j} + \rho b_i = \rho \dot{v}_i \tag{4.1}$$

the boundary condition are given by:

$$n_j \sigma_{ij} = \bar{t}_i \quad \text{on} \quad \Gamma_{t_i} \quad \text{and} \quad [n_j \sigma_{ji} = 0] \quad \text{on} \quad \Gamma_{int}. \tag{4.2}$$

In the finite element method, all the strong form converted to the weak form. Weak form of equation 4.1 in terms of virtual power given as:

$$\int_\Omega \frac{\partial(\delta v_i)}{\partial x_j} \sigma_{ji} d\Omega - \int_\Omega \delta v_i \rho b_i d\Omega - \sum_{i=1}^{n_{SD}} \int_{\Gamma_{t_i}} \delta v_i \bar{t}_i d\Gamma + \int_\Omega \delta v_i \rho \dot{v}_i d\Omega = 0. \tag{4.3}$$

Here, the first term is the virtual internal power, δP^{int}:

$$\delta P^{int} = \int_\Omega \frac{\partial(\delta v_i)}{\partial x_j} \sigma_{ji} d\Omega = \int_\Omega \delta D_{ij} \sigma_{ij} d\Omega = \int_\Omega \delta L_{ij} \sigma_{ij} d\Omega \tag{4.4}$$

the second and third term is virtual external power, δP^{ext}:

$$\delta P^{ext} = \int_\Omega \delta v_i \rho b_i d\Omega + \sum_{i=1}^{n_{SD}} \int_{\Gamma_{t_i}} \delta v_i \bar{t}_i d\Gamma \tag{4.5}$$

the forth term is the virtual kinetic power, δP^{kin}:

$$\delta P^{kin} = \int_\Omega \delta v_i \rho \dot{v}_i d\Omega. \tag{4.6}$$

Here, the velocity gradient L_{ij} is given as:

$$L_{ij} = v_{i,j} = v_{iI} \frac{\partial N_1}{\partial x_j} \tag{4.7}$$

L_{ij} is divided into a symmetric part as the rate of deformation D and a asymmetric

part as the spin tensor W. Here, D and W tensors are given as:

$$D_{ij} = \frac{1}{2}(L_{ij} + L_{ji}) \quad \text{and} \quad W_{ij} = \frac{1}{2}(L_{ij} - L_{ji}). \tag{4.8}$$

Finite element approximation for the Lagrangian formulation is discussed in this section. For this motive, the current domain Ω is divided into elements Ω_e. Current configuration denoted as x_{iI} where I is node number from 1 to n_N and i is for dimension space. In the finite element method, the motion x($\mathbf{X}$,t) is approximated by:

$$x_i(\mathbf{X}, t) = N_I(\mathbf{X}) x_{iI}(t) \tag{4.9}$$

where $N_I(\mathbf{X})$ are the shape function, and x_I is the position vector. For initial position $\mathbf{X}_J$ equation 4.9 is written as:

$$x_i(\mathbf{X}_J, t) = x_{iI}(t) N_I(\mathbf{X}_J) = x_{iJ}(t); \quad \text{where}, N_I(\mathbf{X}_J) = \delta_{IJ}. \tag{4.10}$$

Nodal Displacement field is given as:

$$u_i(\mathbf{X}, t) = x_i(\mathbf{X}, t) - X_i = u_{iI}(t) N_I(\mathbf{X}). \tag{4.11}$$

By taking the material time derivative of the displacement, velocity is given by:

$$v_i(\mathbf{X}, t) = \frac{\partial u_i(\mathbf{X}, t)}{\partial t} = v_{iI}(t) N_I(\mathbf{X}). \tag{4.12}$$

The acceleration is given by the material time derivative of the velocities:

$$a(\mathbf{X}, t) = \dot{v}_{iI}(t) N_I(\mathbf{X}). \tag{4.13}$$

By substituting equation 4.12 into equation 4.3 the discrete finite element equation can be given by:

$$\int_\Omega \frac{\partial N_I}{\partial x_j} \sigma_{ji} \, d\Omega - \int_\Omega N_I \rho b_i \, d\Omega - \sum_{j=1}^{n_{SD}} \int_{\Gamma_{t_j}} N_I \bar{t}_i \, d\Gamma + \int_\Omega N_I \rho \dot{v}_i \, d\Omega = 0; \quad \forall (I, i) \notin \Gamma_{v_i}. \tag{4.14}$$

Internal nodal forces or a stress in a body are given by:

$$f_{iI}^{int} = \int_\Omega \frac{\partial N_{iI}}{\partial x_j} \sigma_{ji} \, d\Omega \tag{4.15}$$

and external nodal forces are given by:

$$f_{iI}^{ext} = \int_{\Omega} N_I \rho b_i \, d\Omega + \int_{\Gamma_{t_i}} N_1 \bar{t}_i \, d\Gamma. \tag{4.16}$$

The kinetic nodal forces are defined by:

$$f_{iI}^{kin} = \int_{\Omega} \rho N_I N_J \, d\Omega \dot{v}_{iJ}. \tag{4.17}$$

Kinetic nodal forces are a product of mass matrix and the nodal acceleration. Mass matrix is defined as:

$$M_{ijIJ} = \delta_{ij} \int_{\Omega} \rho N_I N_J d\Omega. \tag{4.18}$$

So finally, equation of motion can be described as:

$$M_{ijIJ} \dot{v}_{ij} + f_{iI}^{int} = f_{iI}^{ext} \tag{4.19}$$

or

$$Ma + f^{int} = f^{ext}. \tag{4.20}$$

For transient thermal problem the semi-discrete finite element equation for heat transfer can be given by:

$$C_{ij}\dot{\theta}_j + K_{ij}\theta_j = q_i \tag{4.21}$$

heat capacity matrix

$$C_{ab} = \int_{B_t} \rho c N_a N_b dV \tag{4.22}$$

heat conductivity matrix

$$K_{ab} = \int_{B_i} k N_{a,i} N_{b,i} dV. \tag{4.23}$$

Here, c is heat capacity, ρ is mass density, and k is thermal conductivity of the material.

In this study, the explicit method is used for solving the non-linear problem, and the central difference method is the most popular explicit method in computational mechanics. Central difference method for Lagrangian mesh is discussed in this section. The stable time step for Lagrangian mesh changes as the mesh deforms and wave

speed changes. Time increments are defined by:

$$\Delta t^{n+1/2} = t^{n+1} - t^n, \quad t^{n+1/2} = \frac{1}{2}(t^{n+1} + t^n), \quad \Delta t^n = t^{n+1/2} - t^{n-1/2}. \tag{4.24}$$

The central difference formula for velocity is given as:

$$v^{n+1} = \frac{1}{\Delta t^{(n+1/2)}}(d^{n+1} - d^n) \tag{4.25}$$

the acceleration in the term of displacement is given by:

$$a^n = \frac{(d^{n+1} - 2d^n + d^{n-1})}{(\Delta t^n)^2}. \tag{4.26}$$

Equation 4.20 at time step n is given by:

$$Ma^n = f^n = f^{ext}(d^n, t^n) - f^{int}(d^n, t^n). \tag{4.27}$$

Step involved in the explicit time integration

1. Set initial conditions.
2. Calculate force.
3. Compute acceleration: $a^n = M^{-1}(f^n - C^{damp}v^{n-1/2})$.
4. Update time step.
5. Update first partial nodal velocity: $v^{n+1/2} = v^n + (t^{n+1/2} - t^n)a^n$.
6. Enforce velocity BC on node I on Γ^{vi}: $v_{iI}^{n+1/2} = \bar{v}_i(x_I, t^{n^+1/2})$.
7. Update nodal displacement: $d^{n+1} = d^n + \Delta t^{n+1/2}v^{n+1/2}$.
8. Compute force, a^{n+1}, and v^{n+1}.
9. Go to step 4 until require output is obtained.

For explicit method stability criteria is required, and the critical time step can be defined by:

$$\Delta t = \alpha \Delta t_{crit}\,; \quad \Delta t_{crit} \leq \frac{2}{\omega_{max}} = min\Big(\frac{L_e}{c_e}\Big) \tag{4.28}$$

where ω_{max} is the maximum frequency of the linearized system, L_e is a characteristic length and c_e is the current effective wave speed of the element.

4.3 Workpiece and Tool Modeling

The model in this study is defined as a plane strain problem. In orthogonal machining, uncut chip thickness is smaller compared to the depth of cut so this problem can be considered as a plane strain problem. Fig. 4.1 shows the tool-workpiece model used in the study. Tool and workpiece geometry are adopted from [66]. Machining parameters used in this model are listed in Table 4.1.

All the surface node of the tool were constrained in the Y-direction and were giving velocity in the negative X-direction as cutting speed. Nodes on the left and bottom edge of workpiece were constrained in all directions. The initial temperatures for the model is considered as 25°C

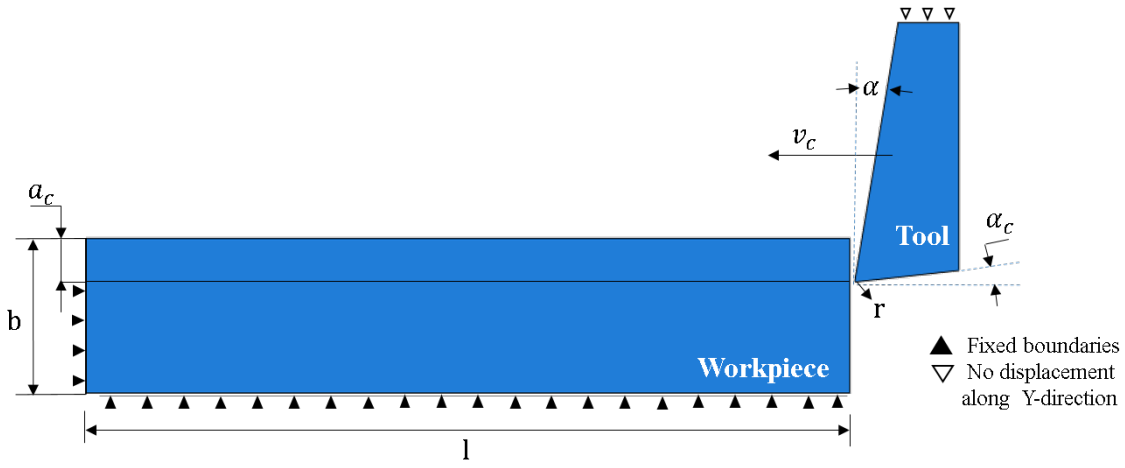

Figure 4.1: Tool- Workpiece.

4.4 Workpiece and Tool Properties

In this model, AISI 1045 steel is used for workpiece material and the tool is constructed of uncoated cemented carbide. Table 4.2 provides chemical composition of AISI 1045 steel. Table 4.3 gives thermo-mechanical properties of workpiece and tool adopted from [67].

Table 4.1: Dimensions of the model

Length of the workpiece (l)	12 mm
Width of the workpiece (b)	1.2 mm
Uncut chip thickness (a_c)	0.1 to 0.3 mm
Tool rake angle (α)	$-7°$ to $10°$
Tool clearance angle (α_c)	$6°$
Tool edge radius (r)	10 µm

Table 4.2: Chemical composition of AISI 1045 carbon steel

Element	C	Mn	S	P	Fe
Content (%)	0.43-0.50	0.60-0.90	0.05	0.04	Balanced

Table 4.3: Thermo- physical properties of Workpiece and tool

Property	Workpiece AISI 1045 steel	Tool Uncoated cemented carbide
Density, ρ (kg/m^3)	7850	14500
Young's modulus, E (GPa)	215 ($20°C$) 210 ($200°C$) 165 ($400°C$) 160 ($600°C$)	534 ($20°C$)
Poisson's ratio, ν	0.3	0.22
Conductivity, κ (W/m°C)	45.04 - 0.021$\times T$	35.95 + 0.042$\times T$
Specific heat, C_p (J/kg°C)	486	334.01 + 0.12$\times T$
Expansion, α_d (µm/m°C)	10.56 + 0.007$\times T$	-

4.5 Meshing in the Geometry

Entire tool-workpiece geometry is divided into small finite element parts. Machining operation demands very complex thermo-mechanical coupling and high strain rate, so it is essential to select the right elements to get an accurate result from the simulation. To model fully coupled thermal-structural problem, four node quadrilateral element with reduced integration, plane strain formulation and hour glass control,

CPE4RT, and three node triangular elements, CPE3T are used in meshing of tool and workpiece.

The total number of elements and nodes used in meshing are 24836 and 25204, respectively. To increase the accuracy of the result in the deformation zone, mesh density is finer in the upper half of the workpiece, as shown in Fig. 4.2a. However, mesh density is coarser in the lower half to reduces the computational time and cost. For the same reason, mesh density in the lower part of the tool is finer, and it is coarser in the upper part, as shown in Fig. 4.2b.

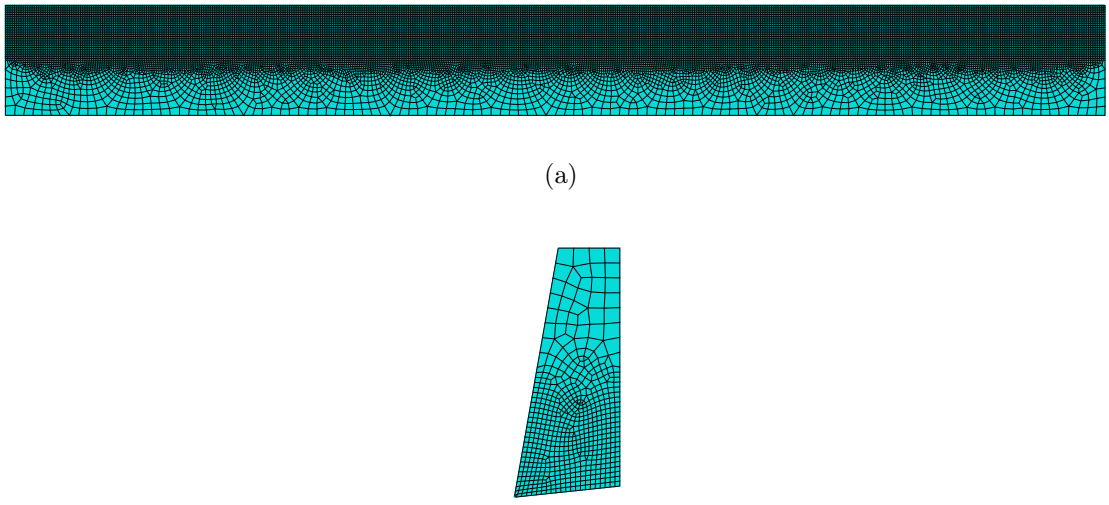

(a)

(b)

Figure 4.2: Meshed geometry (a) workpiece (b) tool.

4.6 Contact Pair Modeling

Contact pair interaction is an essential part of machining modeling. In this study, we have defined two interactions in the model. Self contact with a chip and surface to surface contact between workpiece nodes and the tool surface are established with the kinematic contact model. Surface with coarser mesh or surface of the stiffer body is always treated as master surface. Here workpiece is considered as a slave surface and tool as a master surface. Slave nodes cannot penetrate the master surface, but the nodes of the master surface can penetrate the slave surface [55].

CHAPTER 5: VALIDATION AND VERIFICATION

A numerical model always involves some level of approximation from the experimental model. FEA simulation has been conducted for orthogonal machining for parameters given in table 4.1. By applying UL boundary conditions to the model cutting force, the tool-chip interface temperature, and the chip morphology are evaluated and compared with the experimental data in this chapter to validate the proposed FEA model.

5.1 Force Validation

The simulated cutting forces were compared with the literature and were found in agreement. It can be observed that the cutting force increases as the uncut chip thickness increases. Experimental results by Ivester et al. [68] and FEA results by Karpat et al. [21] for rake angle 5° and -7° are compared with simulated results in Fig. 5.1, and Fig. 5.2. Experimental results by Duan et al. [69] and FEA results by Iqbal et al. [67] are compared with simulated results in Fig. 5.3 for rake angle 0°. From Fig. 5.1b and Fig. 5.2b it can be seen that the percentage difference between experimental and simulated results is around 4-12% compared to the other FEA model [21], which is around 6-18%.

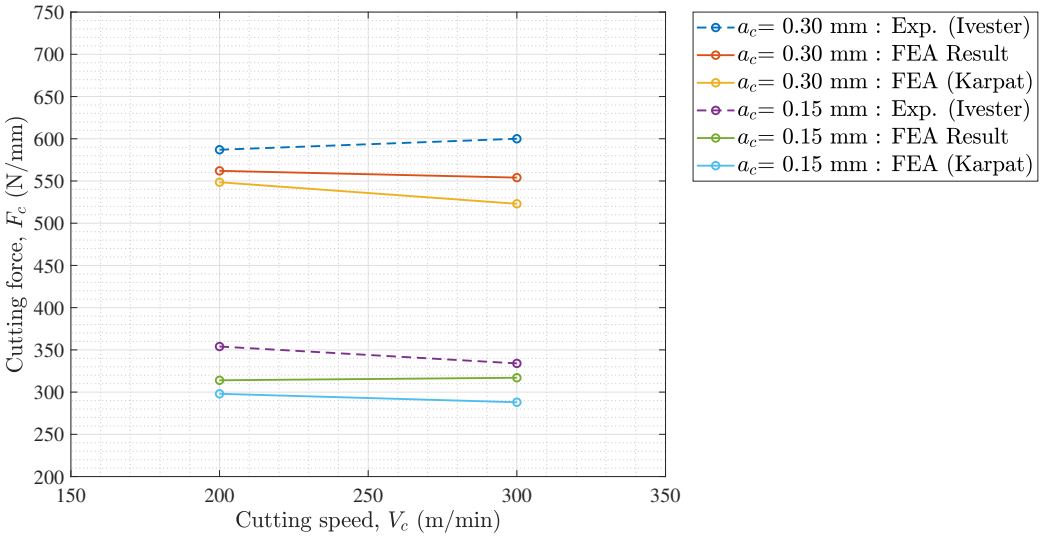

(a)

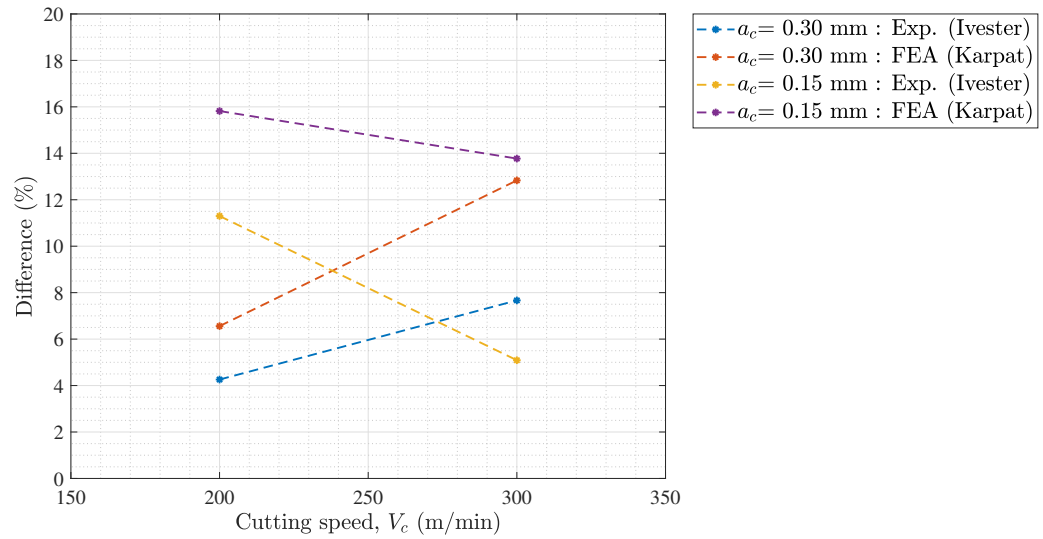

(b)

Figure 5.1: (a) Comparison of simulated average cutting force F_c with the experimental data (b) percentage difference between experimental and simulated cutting forces at $\alpha = 5^\circ$ for various a_c and V_c.

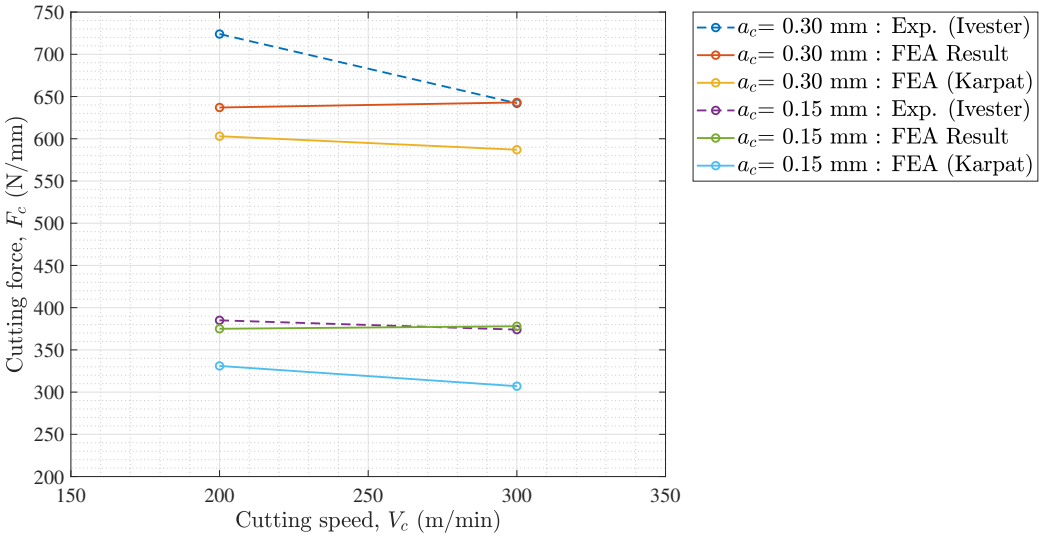

(a)

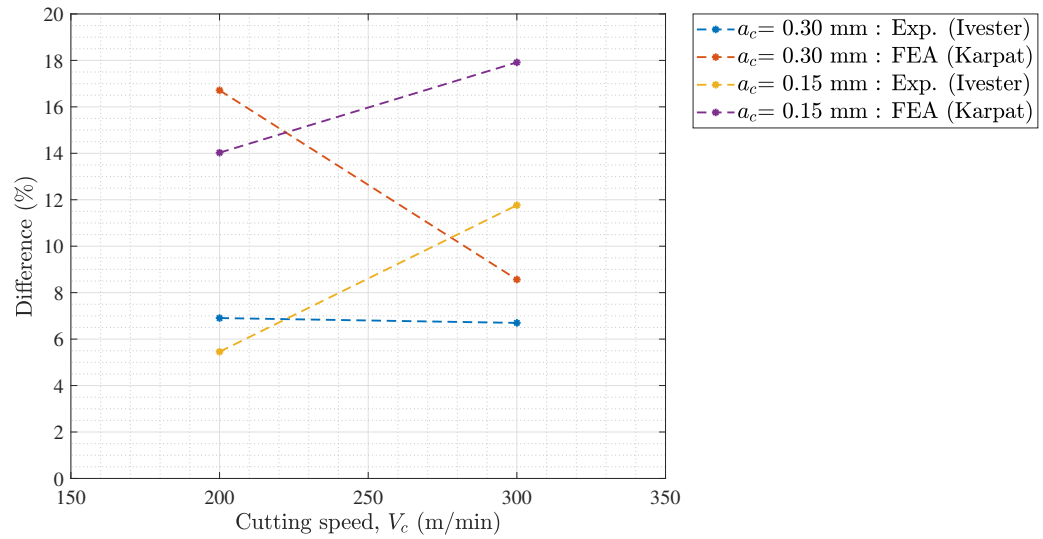

(b)

Figure 5.2: (a) Comparison of simulated average cutting force F_c with the experimental data (b) percentage difference between experimental and simulated cutting forces at $\alpha = -7°$ for various a_c and V_c.

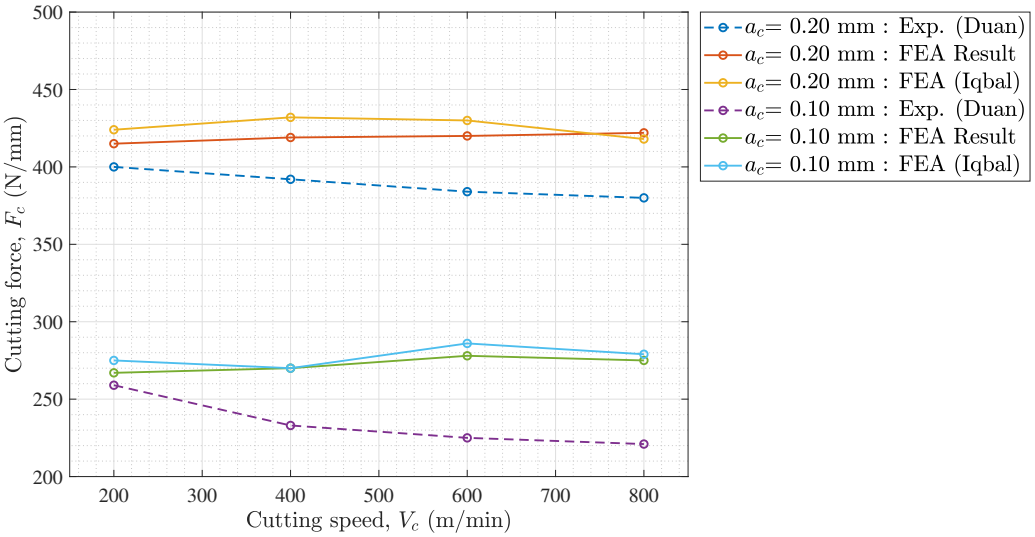

(a)

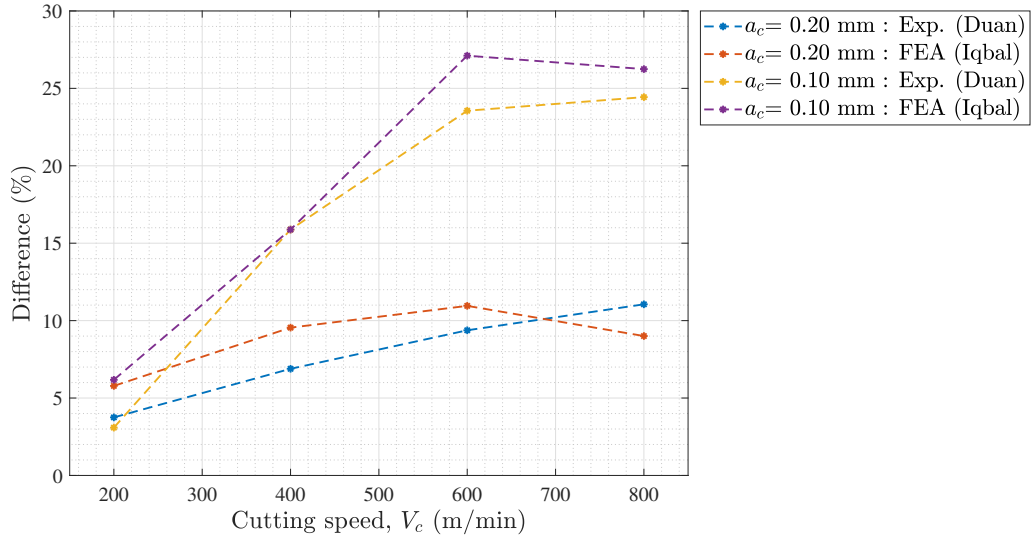

(b)

Figure 5.3: (a) Comparison of simulated average cutting force F_c with the experimental data (b) percentage difference between experimental and simulated cutting forces at $\alpha = 0°$ for various a_c and V_c.

5.2 Temperature Validation

Orthogonal machining at very high speeds generates a large amount of heat due to large deformation and friction between tool and workpiece. This generated heat in the shear zone is conducted into the workpiece, chip, and tool. Temperature field distribution is measured along the contact length for different machining parameters and compared with experimental data in this section. To ensure the validation of the model, numerical results of temperature are compared to the experimental results by Grzesik et al. [70] in table 5.1. Relative error found between results is 8%.

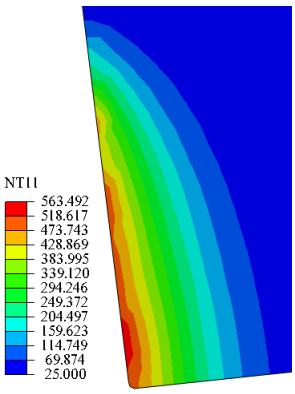

Figure 5.4: Numerical temperature distribution in the tool (°C) for $\alpha = -7°$, $V_c = 200$ m/min, and $a_c = 0.15$ mm.

Table 5.1: Comparison between the numerical and experimental result from the literature

Parameters	Numerical result	Grzesik et al.[70]
Workpiece	AISI 1045 steel	AISI 1045 steel
Tool	Uncoated carbide	Uncoated Carbide
Uncut chip thickness, a_c	0.15 mm	0.16 mm
Rake angle, α	$-7°$	$-5°$
Tool clearance angle, α_c	5°	6°
Cutting Speed, V_c	200 m/min	220 m/min
T_{mean}	470°C	510°C

5.3 Chip Morphology Comparison

The micro structure of the chips obtained experimentally is shown in Fig. 5.5a, 5.6a, and 5.7a [60]. In Fig. 5.5 simulated chip morphology is similar to the experimental result, but Fig. 5.6 and 5.7 give different results than the experiments. The main reason for the inaccurate chip morphology in this study is that accurate Johnson-Cook damage model parameters are not available and the serration on the chip at higher cutting speeds could not be simulated.

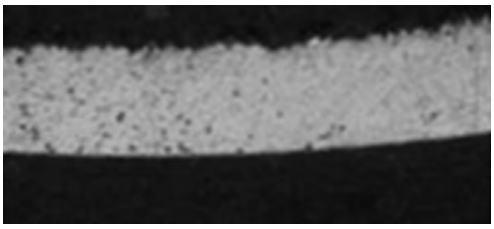

(a)

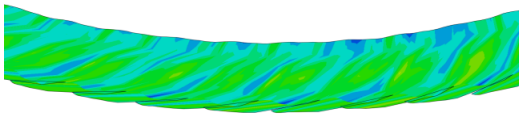

(b)

Figure 5.5: Comparison between chip morphology (a) experimental result (b) simulated result for $a_c = 0.1$ mm, $V_c = 200$ m/min and $\alpha = 0°$.

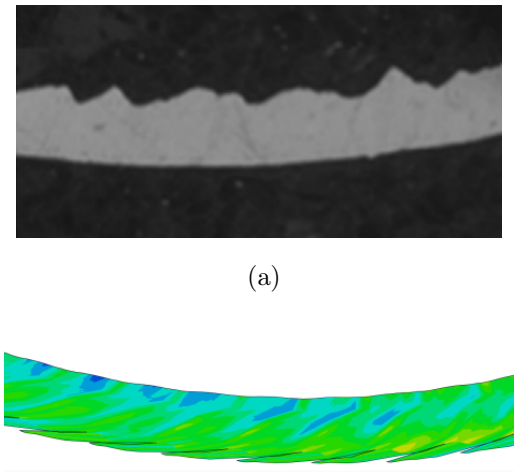

(a)

(b)

Figure 5.6: Comparison between chip morphology (a) experimental result (b) simulated result for $a_c = 0.1$ mm, $V_c = 400$ m/min and $\alpha = 0°$.

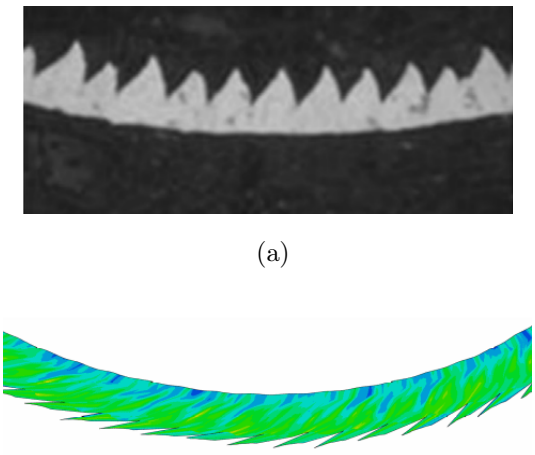

(a)

(b)

Figure 5.7: Comparison between chip morphology (a) experimental result (b) simulated result for $a_c = 0.1$ mm, $V_c = 800$ m/min and $\alpha = 0°$.

CHAPTER 6: NUMERICAL RESULTS AND DISCUSSION

6.1 Force Distribution

To consider the performance of the cutting simulation in this parametric study four different uncut chip thicknesses, rake angles, and cutting velocities are considered. The cutting forces are calculated by adding the reaction forces of the boundary nodes along the bottom and left side of the workpiece. Fig. 6.1 and Fig. 6.2 shows simulated cutting force versus simulated time for rake angle 5° and 0°, uncut chip thickness 0.1 mm, and cutting speed 200 m/min; the average simulated cutting force is, $F_c \approx 251$N and $F_c \approx 227$N respectively. The simulated cutting force with varying cutting speed and rake angle for different uncut chip thicknesses of 0.1, 0.15, 0.2, and 0.3 mm are plotted in Fig. 6.3. In this figure we can see that the cutting force increases as the rake angle decreases from 10° to −7°. Positive rake angle produces higher shear angle, therefor it helps to reduce cutting force. Furthermore, as shown in Fig. 6.4, cutting force increases with an increases in the uncut chip thickness because more energy is required to deform a thicker chip. It also shows that the cutting velocity does not have much effect on the cutting force in orthogonal cutting analysis.

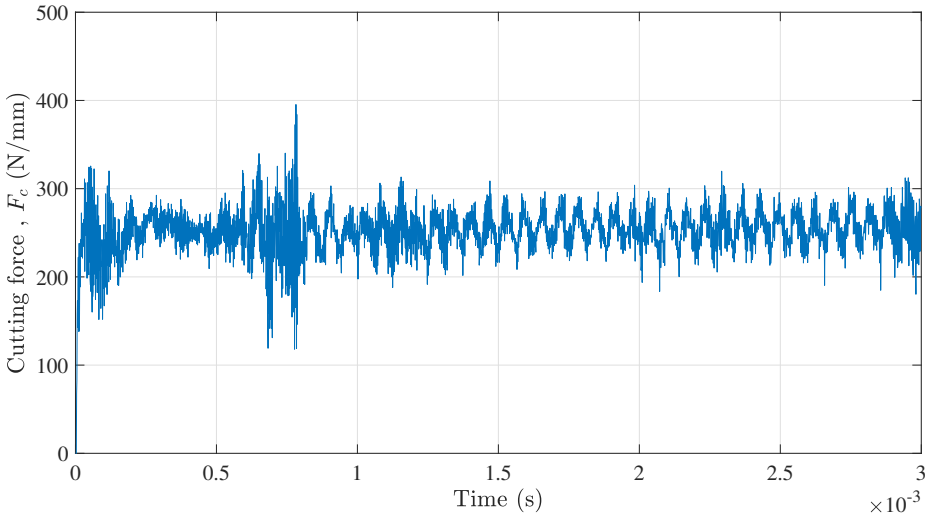

Figure 6.1: Cutting force evolution versus time for $\alpha = 5°$, a_c= 0.1 mm, and V_c= 200 m/min.

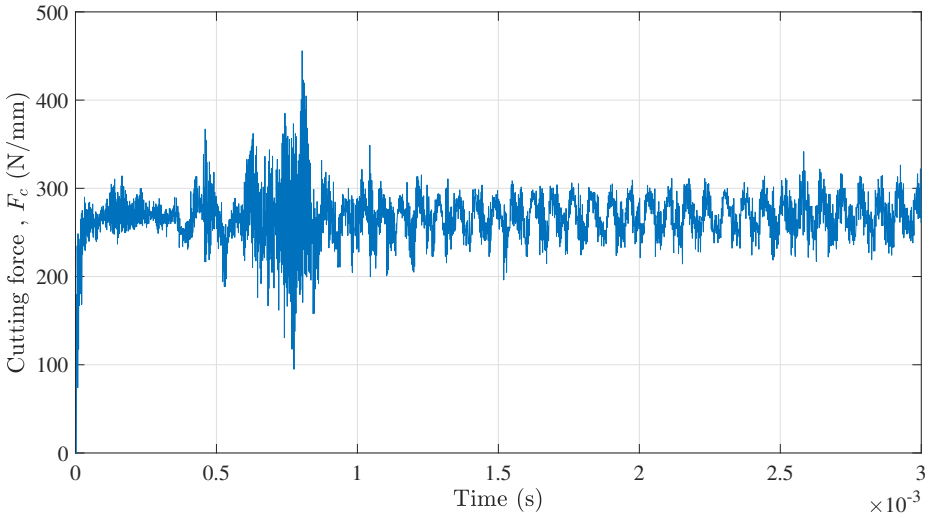

Figure 6.2: Cutting force evolution versus time for $\alpha = 0°$, a_c= 0.1 mm, and V_c= 200 m/min.

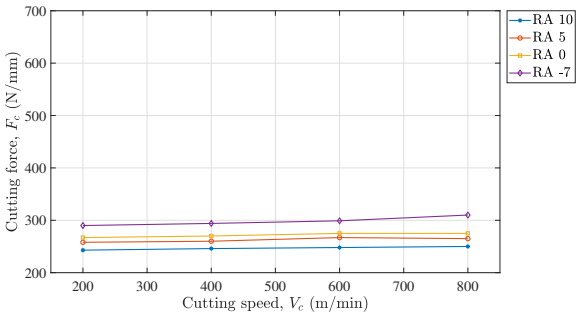

(a)

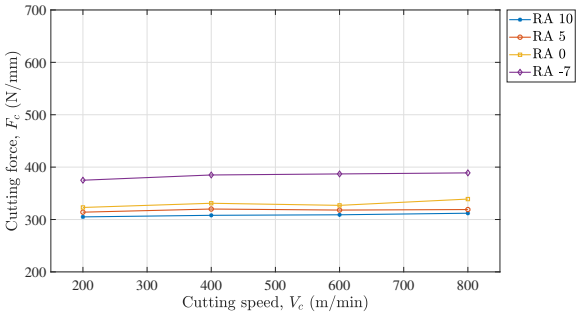

(b)

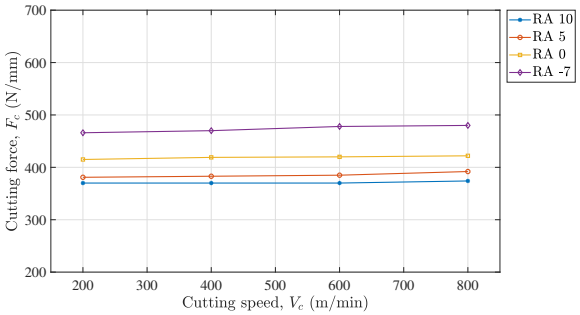

(c)

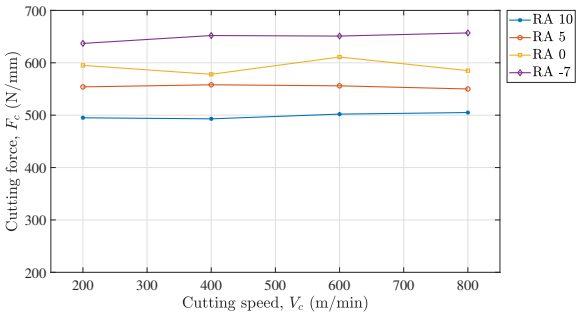

(d)

Figure 6.3: Average cutting force results at uncut chip thickness (a) $a_c = 0.1$ mm (b) $a_c = 0.15$ mm (c) $a_c = 0.2$ mm (d) $a_c = 0.3$ mm for various values of α and V_c.

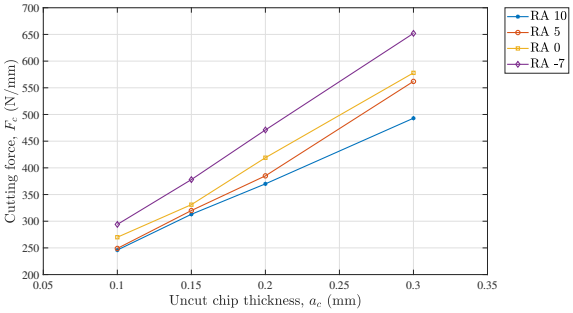

(a)

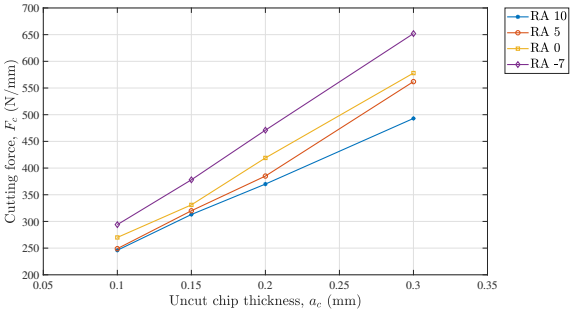

(b)

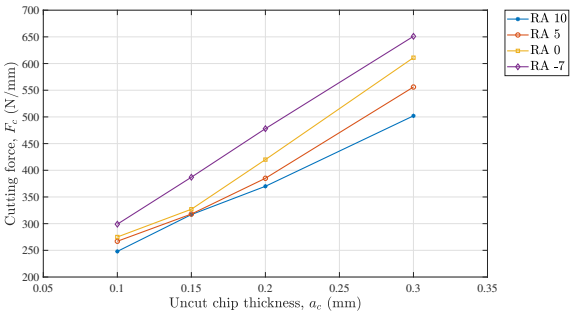

(c)

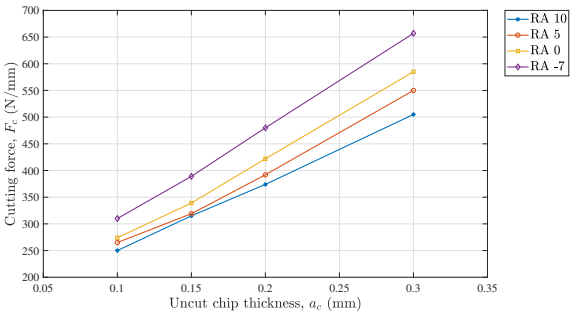

(d)

Figure 6.4: Average cutting force results at cutting speed (a) V_c = 200 m/min (b) V_c = 400 m/min (c) V_c = 600 m/min (d) V_c = 800 m/min for various values of α and a_c.

6.2 Temperature Distribution

In machining, plastic work in the primary shear zone and friction at tool-chip interface mainly contribute in the temperature rise. In this section the trends in temperature with various cutting speeds, tool rake angles, and uncut chip thicknesses are discussed.

Interface temperature at tool-chip is calculated by averaging the nodal temperature along the contact length of the tool. Nodes of contact length are selected to calculate average temperature at the tool-chip interface, as shown in Fig. 6.5. Also Fig. 6.6 shows simulated interface temperature at tool-chip verses time for rake angle $-7°$, uncut chip thickness 0.3 mm, and cutting speed 800 m/min; the average interface temperature at tool-tip is, $T_{\text{mean}} \approx 580°$.

The temperature obtained from finite element simulation of orthogonal machining of AISI 1045 steel are shown in Fig. 6.7 and Fig. 6.8. From Fig. 6.7 it can be concluded that, at the same uncut chip thickness, the interface temperature of the tool-chip increases when the cutting speed increases. In the literature, it shows that

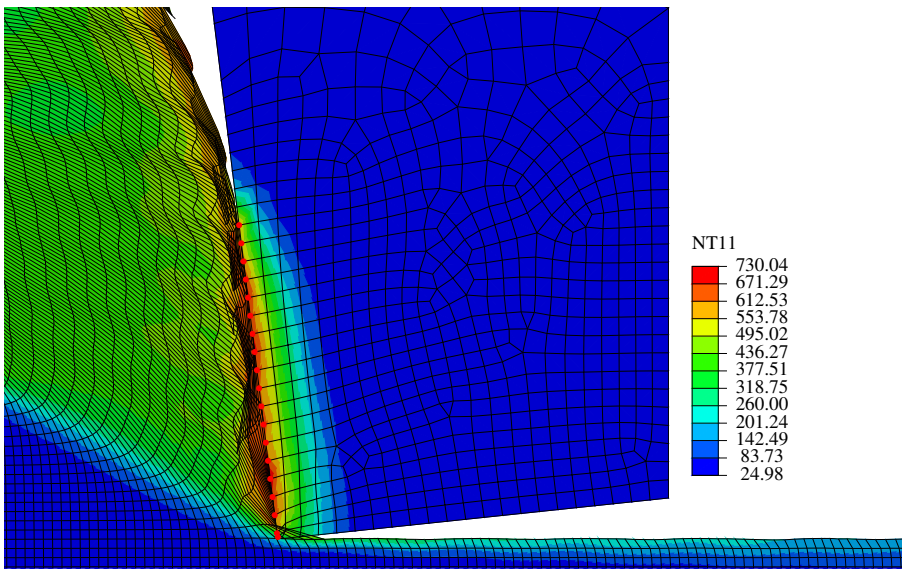

Figure 6.5: Node selection of contact length for calculating average interface temperature.

heat generation increases as cutting speed increases. Also, Fig. 6.8 shows that, at the same cutting speed, the temperature at contact length of the tool increases as the uncut chip thickness increases. Due to increased material removal on the workpiece more mechanical energy converts to heat energy.

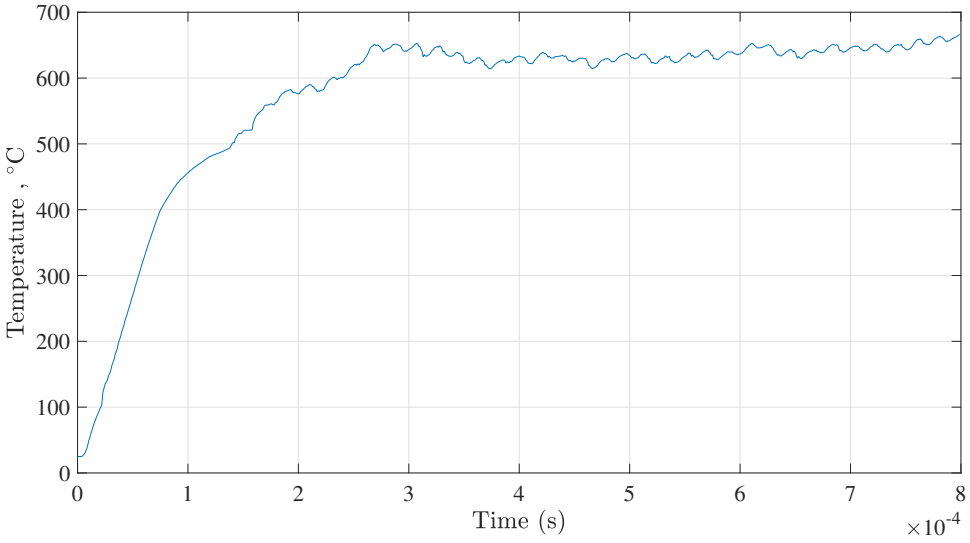

Figure 6.6: Tool chip interface temperature evolution versus time for $\alpha = -7°$, a_c= 0.3 mm, and V_c= 800 m/min.

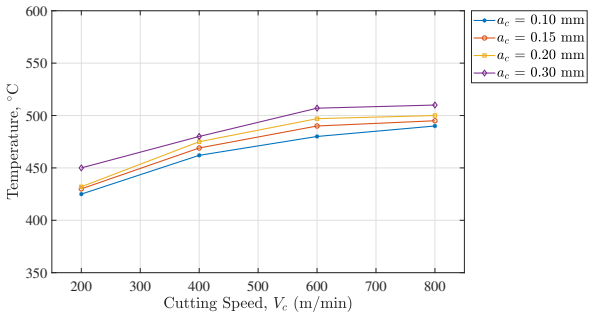

(a)

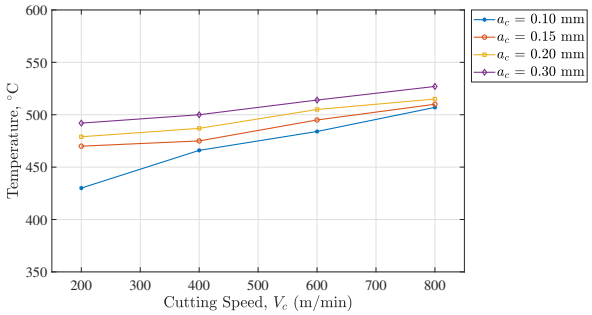

(b)

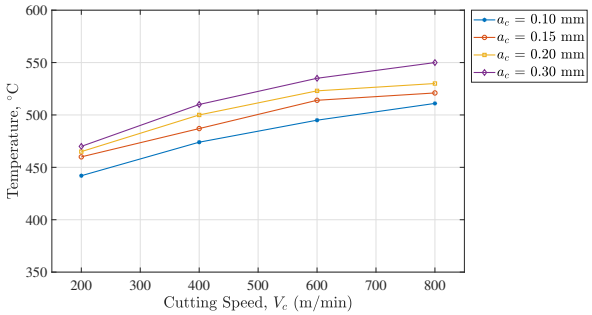

(c)

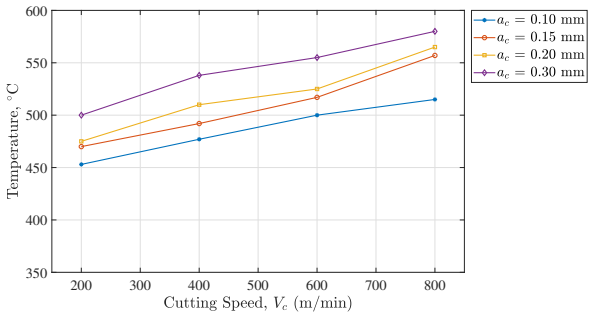

(d)

Figure 6.7: Average chip-tool interface temperature results at rake angle (a) $\alpha = 10°$ (b) $\alpha = 5°$ (c) $\alpha = 0°$(d) $\alpha = -7°$ for various values of a_c and V_c.

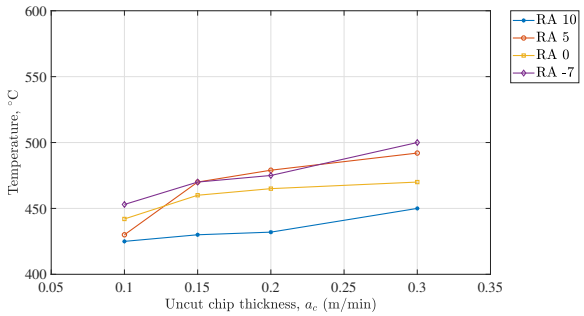

(a)

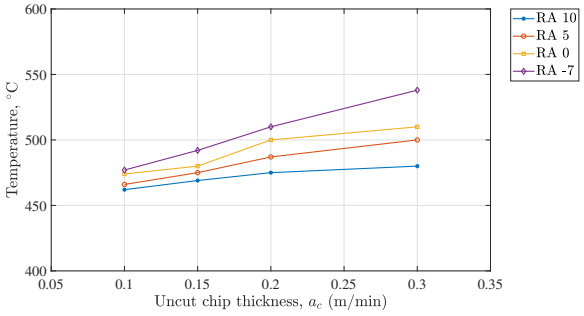

(b)

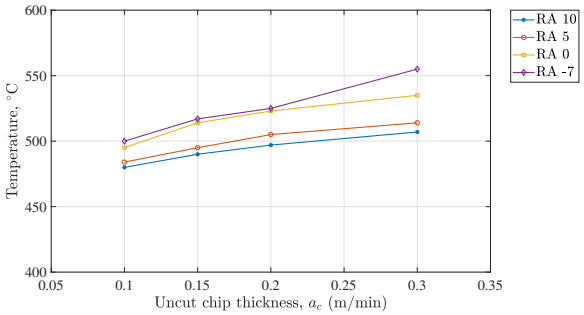

(c)

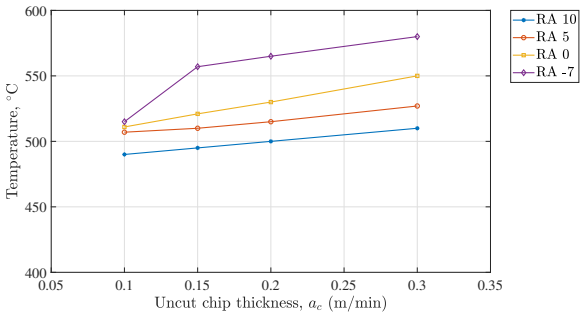

(d)

Figure 6.8: Average chip-tool interface temperature results at cutting speeds (a)V_c = 200 m/min (b) V_c= 400 m/min (c) V_c=600 m/min (d) V_c=800 m/min for various values of a_c and α.

6.3 Comparison of SDEG for Two Different Sets of Johnson-Cook Parameters

The Johnson-Cook damage parameters affect the fracture damage in the chip, and from Fig. 6.9 we can see that the SDEG (overall scalar stiffness degradation variable) parameters are not evident on the external chip interface while using the Johnson-Cook damage data set-II. However, while using the Johnson-Cook damage data set-I damage around the outer chip interface is noted.

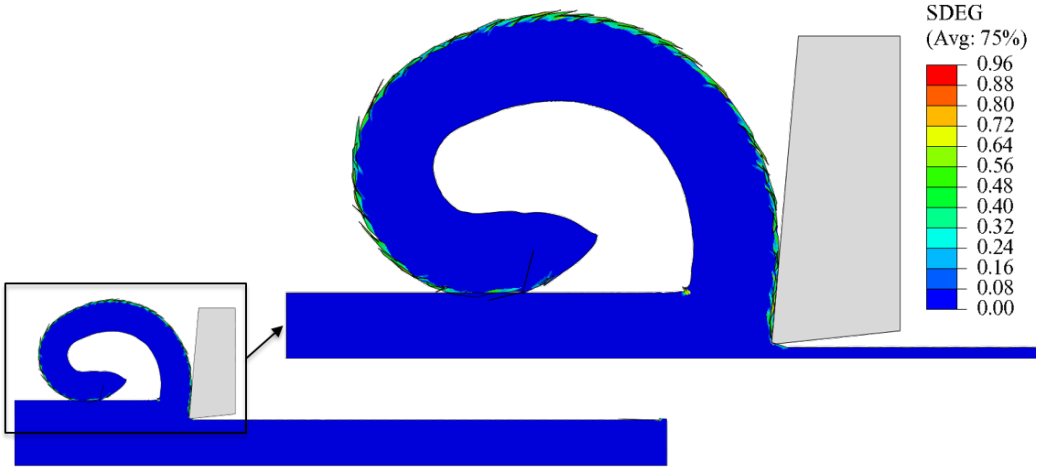

(a)

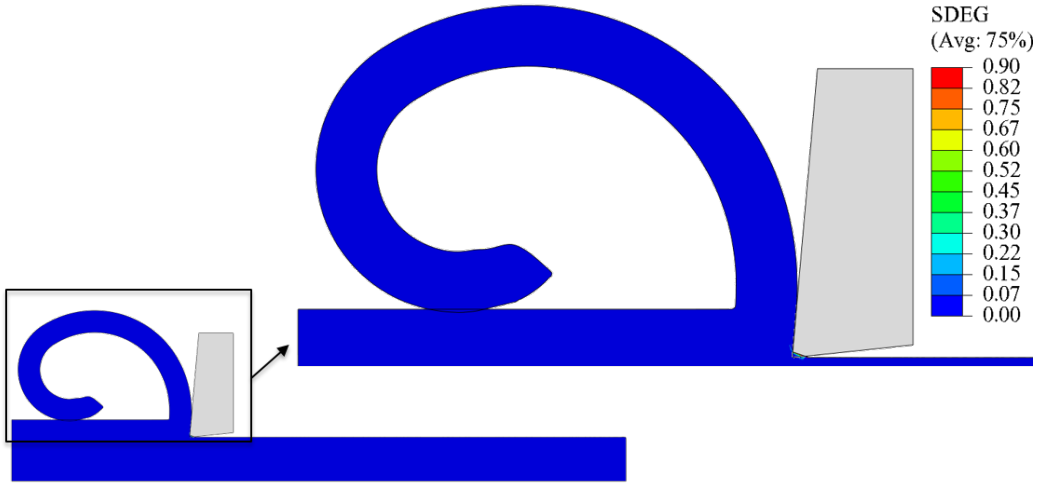

(b)

Figure 6.9: SDEG results (a) Johnson-Cook parameters- I (b) Johnson-Cook parameters - II for $\alpha = 5$, $a_c = 0.3$ mm, and $V_c = 800$ m/min.

From Fig. 6.10 it can conclude that the Johnson-Cook damage data set-I gives more accurate cutting force results than the Johnson-Cook damage data set-II, and the difference is the range of 6-8% compared to the 18-20% difference. So, using correct Johnson-Cook damage parameters in the orthogonal cutting analysis is crucial.

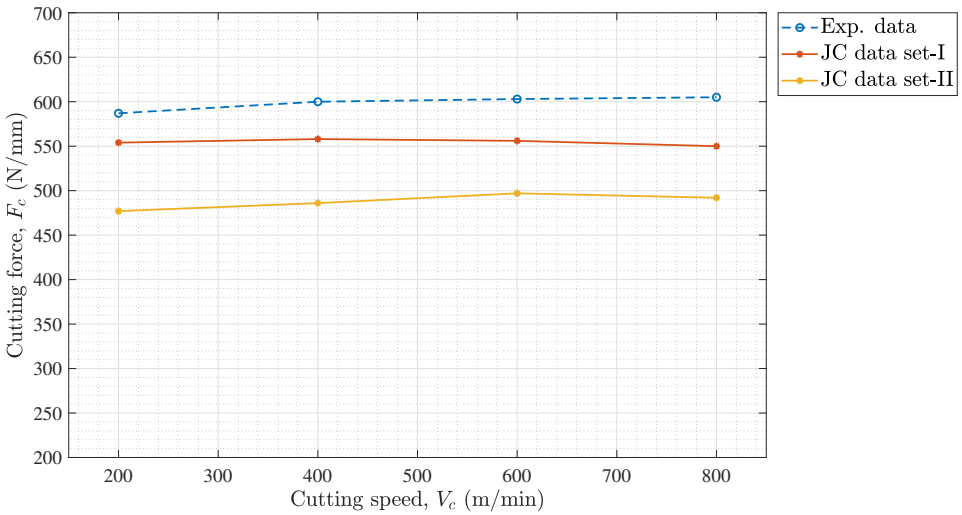

(a) Comparison of predicted average cutting force F_c with the experimental data at $\alpha = 5°C$ for various V_c

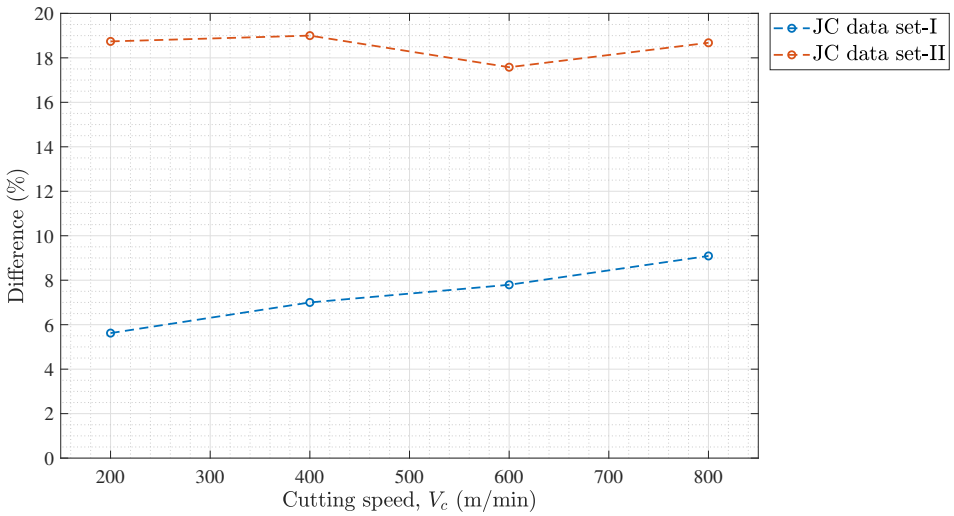

(b) Relative difference between experimental and predicted cutting forces at $\alpha = 5°$ for various V_c

Figure 6.10: Comparison of average cutting force F_c to experimental forces.

6.4 Change in Fracture Toughness for Chip Serration, G_f^{serr}

As discussed earlier, fracture toughness for chip serration is a crucial aspect in orthogonal cutting. As shown in Fig. 6.11 simulation results varied according to G_f^{serr}. As shown in Fig. 6.11a and 6.11c, higher stress and deformation in model caused failure in the simulation for values other than the prescribed value of G_f^{serr}. However, Fig. 6.11b $G_f^{serr} = 24000$ J/m^2 gives an accurate and complete simulation.

(a)

(b)

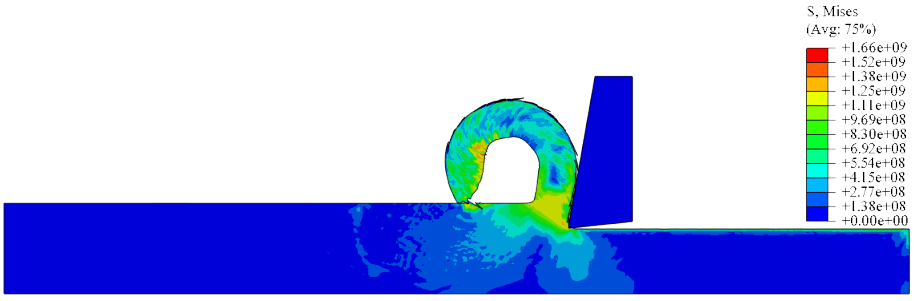

(c)

Figure 6.11: Different chip morphology for different (a) $G_f^{serr} = 20000$ J/m^2 (b) $G_f^{serr} = 24000$ J/m^2 (c) $G_f^{serr} = 28000$ J/m^2, for G_f^{sep}= 14000J/m^2, $\alpha = 10°$, $a_c = 0.3$ mm, and $V_c = 800$ m/min.

CHAPTER 7: CONCLUSION AND FUTURE WORK

7.1 Conclusion

In this thesis, a new model of orthogonal metal cutting is developed using Update Lagrangian finite element approach to simulate chip formation and to identify field variables. It is complex and challenging to model orthogonal machining due to high deformation in the shear zone and high interface temperature. Current development on the fracture mechanics and field damage of ductile material are used in this thesis. The constitutive model, which involves deformation, damage initiation, and damage evolution, is required for accurate modeling; therefore, the Johnson-Cook damage model is used in this study. Johnson-Cook damage parameters-I gives accurate cutting force compare to the data set-II, but to find more precise chip morphology at the high-speed machining we still required accurate Johnson-Cook damage parameters.

Damage evolution model and the criteria used for chip separation and serration is critical in machining model, which need to be accurate for the correct chip morphologies. A threshold value of chip separation and serration are based on the fracture toughness of the material. The values for $G_{\mathrm{f}}^{\mathrm{sep}}$ and $G_{\mathrm{f}}^{\mathrm{serr}}$ are calculated using fracture mechanics, and results are available in the literature.

Zorev's friction model is used with the collaboration of the stress-based friction model, which gives an accurate prediction of the complex friction model phenomena in the study.

The influence of the cutting speed, rake angle, and uncut chip thickness on field variables are studied using uncoated cemented carbide tool. Cutting force increases as the uncut chip thickness increases and rake angle decreases. However, cutting velocity has a minimal effect on the cutting forces. Increases in the cutting speed and

uncut chip thickness raises temperature at the tool-chip interface.

7.2 Future Work

Future works that may extend from this thesis include the following:

The tool life, tool wear, and chip curling can be further studied using this model.

Extension of this two-dimensional finite element model to the three-dimensional model for the oblique cutting process can be modeled.

Accurate Johnson-Cook damage parameters for material AISI 1045 steel is necessary to find for more accurate results at high-speed machining. The proposed model can also be used for different workpiece and tool materials.

Some experiments to identify accurate values of $G_{\mathrm{f}}^{\mathrm{sep}}$ and $G_{\mathrm{f}}^{\mathrm{serr}}$ for AISI 1045 steel are needed to acquire precise results.

More detailed thermal modeling can apply to the tool-chip interface to obtain more accurate thermal results.

Using these parametric studies, one can build a machine learning model for Artificial Neural Network (ANN) or Support Vector Machine (SVM) to predict field variables within a specific range. This approach can reduce computational time and cost in FE modeling.

REFERENCES

[1] C. Kılıçaslan, "Modelling and simulation of metal cutting by finite element method," Master's thesis, izmir institute of technology, 2009.

[2] Z. Liao and D. A. Axinte, "On chip formation mechanism in orthogonal cutting of bone," *International Journal of Machine Tools and Manufacture*, vol. 102, pp. 41–55, 2016.

[3] K. Sheikh, "Non traditional machining," 2011.

[4] V. Piispanen, "Theory of formation of metal chips," *Journal of Applied Physics*, vol. 19, no. 10, pp. 876–881, 1948.

[5] H. Ernst and M. E. Merchant, *Chip formation, friction and finish.* Cincinnati milling machine Company Cincinnati, 1941.

[6] M. E. Merchant, "Mechanics of the metal cutting process. ii. plasticity conditions in orthogonal cutting," *Journal of applied physics*, vol. 16, no. 6, pp. 318–324, 1945.

[7] E. Lee, "The theory of plasticity applied to a problem of machining," *ASME J. Appl. Mech.*, vol. 18, p. 405, 1951.

[8] H. Kudo, "Some new slip-line solutions for two-dimensional steady-state machining," *International Journal of Mechanical Sciences*, vol. 7, no. 1, pp. 43–55, 1965.

[9] P. Dewhurst, "On the non-uniqueness of the machining process," *Proceedings of the Royal Society of London. A. Mathematical and Physical Sciences*, vol. 360, no. 1703, pp. 587–610, 1978.

[10] P. Oxley and M. Welsh, "Calculating the shear angle in orthogonal metal cutting from fundamental stress-strain-strain rate properties of the work material," 1964.

[11] K. Okushima and K. Hitomi, "An analysis of the mechanism of orthogonal cutting and its application to discontinuous chip formation," *Journal of Engineering for Industry*, vol. 83, no. 4, pp. 545–555, 1961.

[12] E. Usui and T. Shirakashi, "Mechanics of machiningâfrom descriptive to predictive theory," *On the Art of Cutting Metals - 75 Years Later*, vol. 7, pp. 13–35, 1982.

[13] J. S. Strenkowski and J. Carroll, "A finite element model of orthogonal metal cutting," *Journal of Engineering for Industry*, vol. 107, no. 4, pp. 349–354, 1985.

[14] Z. Lin and S. Lin, "A coupled finite element model of thermo-elastic-plastic large deformation for orthogonal cutting," *Journal of engineering materials and technology*, vol. 114, no. 2, pp. 218–226, 1992.

[15] A. J. Shih, "Finite element simulation of orthogonal metal cutting," *Journal of engineering for industry*, vol. 117, no. 1, pp. 84–93, 1995.

[16] P. Oxley, "The mechanics of machining: An analytical approach to assessing," *Machinability. Ellis Horwood Ltd., England*, 1989.

[17] T. Shirakashi, "Flow stress of low carbon steel at high temperature and strain rate (part 1, part 2)," *Bull. Japan Soc. Prec. Eng.*, vol. 17, no. 3, p. 161, 1983.

[18] F. J. Zerilli and R. W. Armstrong, "Dislocation-mechanics-based constitutive relations for material dynamics calculations," *Journal of applied physics*, vol. 61, no. 5, pp. 1816–1825, 1987.

[19] S. Jaspers and J. Dautzenberg, "Material behaviour in conditions similar to metal cutting: flow stress in the primary shear zone," *Journal of Materials Processing Technology*, vol. 122, no. 2-3, pp. 322–330, 2002.

[20] T. Özel, "The influence of friction models on finite element simulations of machining," *International Journal of Machine Tools and Manufacture*, vol. 46, no. 5, pp. 518–530, 2006.

[21] Y. Karpat and T. Özel, "Predictive analytical and thermal modeling of orthogonal cutting processâpart i: predictions of tool forces, stresses, and temperature distributions," *Journal of manufacturing science and engineering*, vol. 128, no. 2, pp. 435–444, 2006.

[22] G. R. Johnson, "A constitutive model and data for materials subjected to large strains, high strain rates, and high temperatures," *Proc. 7th Inf. Sympo. Ballistics*, pp. 541–547, 1983.

[23] C. S. Prasad, "Finite element modeling to verify residual stress in orthogonal machining," 2009.

[24] V. Madhavan, S. Chandrasekar, and T. Farris, "Machining as a wedge indentation," *Journal of Applied Mechanics*, vol. 67, no. 1, pp. 128–139, 2000.

[25] J. S. Strenkowski and K.-J. Moon, "Finite element prediction of chip geometry and tool/workpiece temperature distributions in orthogonal metal cutting," *Journal of Engineering for Industry*, vol. 112, no. 4, pp. 313–318, 1990.

[26] K. Komvopoulos and S. Erpenbeck, "Finite element modeling of orthogonal metal cutting," *Journal of engineering for industry*, vol. 113, no. 3, pp. 253–267, 1991.

[27] A. Shih, S. Chandrasekar, and H. Yang, "Finite element simulation of metal cutting process with strain-rate and temperatures effects," *Fundamental Issues in Machining, ASME, PED*, vol. 43, pp. 11–24, 1990.

[28] M. Shatla, C. Kerk, and T. Altan, "Process modeling in machining. part i: determination of flow stress data," *International Journal of Machine Tools and Manufacture*, vol. 41, no. 10, pp. 1511–1534, 2001.

[29] N. Zorev, "Inter-relationship between shear processes occurring along tool face and shear plane in metal cutting," *International research in production engineering*, vol. 49, pp. 143–152, 1963.

[30] M. Dirikolu, T. Childs, and K. Maekawa, "Finite element simulation of chip flow in metal machining," *International Journal of Mechanical Sciences*, vol. 43, no. 11, pp. 2699–2713, 2001.

[31] A. P. Markopoulos, *Finite element method in machining processes*. Springer Science & Business Media, 2012.

[32] A. Simoneau, E. Ng, and M. Elbestawi, "Chip formation during microscale cutting of a medium carbon steel," *International Journal of Machine Tools and Manufacture*, vol. 46, no. 5, pp. 467–481, 2006.

[33] E.-G. Ng, T. I. El-Wardany, M. Dumitrescu, and M. A. Elbestawi, "Physics-based simulation of high speed machining," *Machining science and technology*, vol. 6, no. 3, pp. 301–329, 2002.

[34] A. Tay, M. Stevenson, and G. de Vahl Davis, "Using the finite element method to determine temperature distributions in orthogonal machining," *Proceedings of the institution of mechanical engineers*, vol. 188, no. 1, pp. 627–638, 1974.

[35] T. Childs and K. Maekawa, "Computer-aided simulation and experimental studies of chip flow and tool wear in the turning of low alloy steels by cemented carbide tools," *Wear*, vol. 139, no. 2, pp. 235–250, 1990.

[36] B. Zhang and A. Bagchi, "Finite element simulation of chip formation and comparison with machining experiment," *Journal of engineering for industry*, vol. 116, no. 3, pp. 289–297, 1994.

[37] J. T. Carroll III and J. S. Strenkowski, "Finite element models of orthogonal cutting with application to single point diamond turning," *International Journal of Mechanical Sciences*, vol. 30, no. 12, pp. 899–920, 1988.

[38] J. Xie, A. Bayoumi, and H. Zbib, "A study on shear banding in chip formation of orthogonal machining," *International Journal of Machine Tools and Manufacture*, vol. 36, no. 7, pp. 835–847, 1996.

[39] K. Iwata, K. Osakada, and Y. Terasaka, "Process modeling of orthogonal cutting by the rigid-plastic finite element method," *Journal of Engineering Materials and Technology*, vol. 106, no. 2, pp. 132–138, 1984.

[40] Z. G. Chen and J. Black, "Fem modeling in metal cutting," *Manufacturing Review(USA)*, vol. 7, no. 2, pp. 120–133, 1994.

[41] M. Shaw, "Metal cutting principles 3rd edition," 1957.

[42] A. Atkins, "Modelling metal cutting using modern ductile fracture mechanics: quantitative explanations for some longstanding problems," *International Journal of Mechanical Sciences*, vol. 45, no. 2, pp. 373–396, 2003.

[43] G. I. Taylor and H. Quinney, "The latent energy remaining in a metal after cold working," *Proceedings of the Royal Society of London. Series A, Containing Papers of a Mathematical and Physical Character*, vol. 143, no. 849, pp. 307–326, 1934.

[44] P. Longère and A. Dragon, "Evaluation of the inelastic heat fraction in the context of microstructure-supported dynamic plasticity modelling," *International Journal of Impact Engineering*, vol. 35, no. 9, pp. 992–999, 2008.

[45] P. J. Arrazola *et al.*, "Investigations on the effects of friction modeling in finite element simulation of machining," *International journal of mechanical sciences*, vol. 52, no. 1, pp. 31–42, 2010.

[46] M. A. Davies, Q. Cao, A. Cooks, and R. Ivester, "On the measurement and prediction of temperature fields in machining aisi 1045 steel," *CIRP Annals*, vol. 52, no. 1, pp. 77–80, 2003.

[47] Y.-C. Yen, A. Jain, P. Chigurupati, W.-T. Wu, and T. Altan, "Computer simulation of orthogonal cutting using a tool with multiple coatings," *Machining science and technology*, vol. 8, no. 2, pp. 305–326, 2004.

[48] F. Klocke, H.-W. Raedt, and S. Hoppe, "2d-fem simulation of the orthogonal high speed cutting process," 2001.

[49] L.-J. Xie, J. Schmidt, C. Schmidt, and F. Biesinger, "2d fem estimate of tool wear in turning operation," *Wear*, vol. 258, no. 10, pp. 1479–1490, 2005.

[50] S. Iqbal, P. Mativenga, and M. Sheikh, "An investigative study of the interface heat transfer coefficient for finite element modelling of high-speed machining," *Proceedings of the Institution of Mechanical Engineers, Part B: Journal of Engineering Manufacture*, vol. 222, no. 11, pp. 1405–1416, 2008.

[51] S. Belhadi, T. Mabrouki, J.-F. Rigal, and L. Boulanouar, "Experimental and numerical study of chip formation during straight turning of hardened aisi 4340 steel," *Proceedings of the Institution of Mechanical Engineers, Part B: Journal of Engineering Manufacture*, vol. 219, no. 7, pp. 515–524, 2005.

[52] K. Wang, *Calibration of the Johnson-Cook failure parameters as the chip separation criterion in the modelling of the orthogonal metal cutting process*. PhD thesis, 2016.

[53] G. R. Johnson and W. H. Cook, "Fracture characteristics of three metals subjected to various strains, strain rates, temperatures and pressures," *Engineering fracture mechanics*, vol. 21, no. 1, pp. 31–48, 1985.

[54] M. Vaziri, M. Salimi, and M. Mashayekhi, "A new calibration method for ductile fracture models as chip separation criteria in machining," *Simulation Modelling Practice and Theory*, vol. 18, no. 9, pp. 1286–1296, 2010.

[55] D. Simulia, "Abaqus 6.16 analysis user's manual," *Abaqus*, 2016.

[56] A. Hillerborg, M. Modéer, and P.-E. Petersson, "Analysis of crack formation and crack growth in concrete by means of fracture mechanics and finite elements," *Cement and concrete research*, vol. 6, no. 6, pp. 773–781, 1976.

[57] G. R. Irwin and J. Kies, "Critical energy rate analysis of fracture strength," *Spie Milestone series MS*, vol. 137, pp. 136–141, 1997.

[58] T. Mabrouki, F. Girardin, M. Asad, and J.-F. Rigal, "Numerical and experimental study of dry cutting for an aeronautic aluminium alloy (a2024-t351)," *International Journal of Machine Tools and Manufacture*, vol. 48, no. 11, pp. 1187–1197, 2008.

[59] Y. Abushawashi, X. Xiao, and V. P. Astakhov, "Fem simulation of metal cutting using a new approach to model chip formation," *International journal of advances in machining and forming operations*, vol. 3, no. 2, pp. 71–92, 2011.

[60] B. Wang, Z. Liu, and Q. Yang, "Investigations of yield stress, fracture toughness, and energy distribution in high speed orthogonal cutting," *International Journal of Machine Tools and Manufacture*, vol. 73, pp. 1–8, 2013.

[61] I. Finnie, "The friction process in metal cutting," in *ASME*, vol. 74, p. 61, 1952.

[62] M. Kronenberg, "Machining science and application," 1966.

[63] X. Yang and C. R. Liu, "A new stress-based model of friction behavior in machining and its significant impact on residual stresses computed by finite element method," *International Journal of Mechanical Sciences*, vol. 44, no. 4, pp. 703–723, 2002.

[64] T. Childs, M. Mahdi, and G. Barrow, "On the stress distribution between the chip and tool during metal turning," *CIRP Annals*, vol. 38, no. 1, pp. 55–58, 1989.

[65] T. Belytschko, W. K. Liu, B. Moran, and K. Elkhodary, *Nonlinear finite elements for continua and structures*. John wiley & sons, 2013.

[66] K. Woon, M. Rahman, K. Neo, and K. Liu, "The effect of tool edge radius on the contact phenomenon of tool-based micromachining," *International Journal of Machine Tools and Manufacture*, vol. 48, no. 12-13, pp. 1395–1407, 2008.

[67] S. Iqbal, P. Mativenga, and M. Sheikh, "Characterization of machining of aisi 1045 steel over a wide range of cutting speeds. part 2: evaluation of flow stress models and interface friction distribution schemes," *Proceedings of the Institution*

of Mechanical Engineers, Part B: Journal of Engineering Manufacture, vol. 221, no. 5, pp. 917–926, 2007.

[68] R. Ivester, M. Kennedy, M. Davies, R. Stevenson, J. Thiele, R. Furness, and S. Athavale, "Assessment of machining models: progress report," *Machining Science and Technology*, vol. 4, no. 3, pp. 511–538, 2000.

[69] C. Duan, H. Li, H. Yu, and M. Wang, "Study on cutting force under serrated chip formation and adiabaitic shear instability during high speed turning of aisi 1045 hardened steel," in *2010 International Conference on Mechanic Automation and Control Engineering*, pp. 3290–3293, IEEE, 2010.

[70] W. Grzesik and P. Nieslony, "Thermal characterization of the chip-tool interface when using coated turning inserts," *Journal of Manufacturing Processes*, vol. 2, no. 2, pp. 79–87, 2000.